# Research Repository UCD

| Title | Hydrogeological and geophysical properties of the very-slow-moving Ripley Landslide, Thompson River valley, British Columbia |
|---|---|
| **Authors(s)** | Huntley, David, Holmes, Jessica, Bobrowsky, Peter, Donohue, Shane, et al. |
| **Publication date** | 2020-08-20 |
| **Publication information** | Huntley, David, Jessica Holmes, Peter Bobrowsky, Shane Donohue, and et al. "Hydrogeological and Geophysical Properties of the Very-Slow-Moving Ripley Landslide, Thompson River Valley, British Columbia" 57, no. 12 (August 20, 2020). |
| **Publisher** | Canadian Science Publishing |
| **Item record/more information** | http://hdl.handle.net/10197/12529 |
| **Publisher's version (DOI)** | 10.1139/cjes-2019-0187 |

1    **Hydrogeological and geophysical properties of the very slow-moving Ripley Landslide,**

2    **Thompson River valley, British Columbia**

3    David Huntley[1*], Jessica Holmes[2, 3], Peter Bobrowsky[4], Jonathan Chambers[3], Philip

4    Meldrum[3], Paul Wilkinson[3], Shane Donohue[5], David Elwood[6], Kelvin Sattler[6], Michael

5    Hendry[7], Renato Macciotta[7], and Nicholas Roberts[8]

6    1.  Geological Survey of Canada, Vancouver, Canada

7        * Corresponding author email: david.huntley@canada.ca

8        ** Corresponding author phone: 604-365-6678

9    2.  Queen's University Belfast, Belfast, Northern Ireland

10   3.  British Geological Survey, Nottingham, United Kingdom

11   4.  Geological Survey of Canada, Sidney, Canada

12   5.  University College Dublin, Ireland

13   6.  University of Saskatchewan, Saskatoon, Saskatchewan

14   7.  University of Alberta, Edmonton, Alberta

15   8.  Mineral Resources Tasmania, Department of State Growth, Rosny Park, Australia

16 **Abstract**

17 Landslides along a 10-km reach of Thompson River south of Ashcroft, British Columbia have

18 repeatedly damaged vital railway infrastructure and threaten salmon runs, potable water

19 supplies, cultural heritage features, and public safety. Government agencies, universities and

20 the railway industry are focusing research efforts on a single test site – the very slow-moving

21 Ripley Landslide – to better manage geohazard risk in this corridor. We characterize the

22 landslide's composition through hydrogeological and geophysical mapping. Field mapping and

23 exploratory drilling distinguished ten hydrogeological units in surficial deposits and fractured

24 bedrock. Electrical resistivity tomography, frequency domain electromagnetic conductivity

25 measurements, ground penetrating radar, seismic primary wave refraction and multispectral

26 analysis of shear waves; in conjunction with down-hole measurement of natural gamma

27 radiation, induction conductivity and magnetic susceptibility provide a detailed, static picture

28 of soil moisture and groundwater conditions within the hydrogeological units. Differences in

29 electrical resistivity of the units reflect a combination of hydrogeological characteristics,

30 temperature and solutes. Resistive earth materials include dry glaciofluvial outwash and non-

31 fractured bedrock; whereas glaciolacustrine clay and silt, water-bearing fractured bedrock, and

32 saturated to partly saturated till and outwash are conductive. These new hydrogeological and

33 geophysical datasets enhance understanding of the composition and internal structure of this

34 landslide and provide important context to interpret multi-year monitoring underway in the

35 valley. Continuous real-time monitoring of electrical resistivity, now underway, will help

36 characterize water-flow paths and possible relationships to independently monitor pore

37 pressures and slope creep.

38

**Introduction**

The ten-kilometre stretch of Thompson River between Ashcroft and Basque Ranch, British Columbia (BC) has experienced numerous landslides since the mid-1800s (**Fig. 1**). In light of threats to trans-continental transportation, Stanton (1898) investigated the earliest of these events in one of the first landslide studies in the Canadian Cordillera. Subsequent rapid failures occurred during the twentieth century (Porter et al. 2002; Clague and Evans 2003) and numerous landslides along this reach continue to creep (Eshraghian et al. 2008; Journault et al. 2018). Such instabilities have the potential to impact both of Canada's national railways, portions of Trans-Canada Highway, arable land, fisheries, and the community of Ashcroft (**Fig. 1** a). They also provide insight into landslide risk of several communities similarly situated along the inner gorge of Thompson River such as Spences Bridge, and as far south as Lytton at the confluence with Fraser River, where repeated failures have generated displacement waves or landslide dams (Drysdale 1914; Porter et al. 2002; Clague and Evans 2003).

Since 2013, Ripley Landslide has been used as a research test site to advance understanding of the composition, behaviour, and associated risks of similar but generally larger landslides along this stretch of Thompson River. The landslide occurs in unconsolidated valley fill on the east bank of the river, seven kilometres south of Ashcroft (**Fig. 1** b), and due to the small size (~3.3 ha) and continuous activity, it is an ideal target for geohazard characterization and monitoring (**Fig. 1** c, d; Bobrowsky et al. 2014, 2017). Completed and ongoing investigations at this site focus on monitoring of landslide motion and environmental conditions, through a combination of slope instrumentation, real-time global navigation satellite system (GNSS) tracking, repeat unmanned aerial vehicle (UAV) surveys, and spaceborne RADAR interferometry (InSAR) (Bunce and Chadwick 2012; Macciotta et al. 2014; Hendry et al. 2015; Journault et al. 2018). The resulting insights are guiding future landslide monitoring and geohazard mitigation efforts

66  in the inner gorge of Thompson River and along similar reaches of Fraser River downstream

67  (Bobrowsky et al. 2018).

68

69  To investigate the composition of the landslide, we undertook a field-focused program

70  combining hydrogeological mapping, stratigraphic analysis of borehole logs, geophysical

71  testing (Huntley and Bobrowsky 2014; Huntley et al. 2017a), along with laboratory

72  characterization of sediments and their electrical properties. Based on this work, we here

73  characterize hydrogeological, geophysical variability and electrical properties of Ripley

74  Landslide. These details provide important context for interpreting instrumental and remotely

75  sensed records from the Ripley test site; and for understanding causal mechanisms and function

76  of this and similar landslides along Thompson River.

77

78  **Background: Landslides of the Thompson River Valley**

79  *Physiology, geology and climate*

80  Thompson River occupies a broad, approximately 1 km-deep, locally steep, bedrock valley.

81  Basement rock near Ashcroft comprises various units of the late Paleozoic to early Mesozoic

82  Cache Creek Terrane and the largely Mesozoic Quesnel Terrane that are respectively of oceanic

83  and island arc affinity (Monger and McMillan 1989; Gordey et al. 1991; Beatty et al. 2006).

84  The youngest rocks, predominantly clastic sedimentary rock of the Jurassic Ashcroft

85  Formation, are sporadically exposed along Thompson River for 10 km south of Ashcroft

86  (Monger and McMillan 1989; Beatty et al. 2006). Above ~500 m elevation, slopes are locally

87  mantled by colluvium or drift. Valley-bottom benchlands, reaching up to 350 m elevation, have

88  been incised by Thompson River since the last glaciation, forming an inner gorge with steep

89  slopes up to 125 m high.

90

91  Thick (50 m to 150 m) Pleistocene valley-bottom fill is well exposed along post-glacial terrace

92  scarps of Thompson River and its tributaries (Ryder 1976; Clague and Evans 2003; Johnsen

93  and Brennand 2004). These sediments include multiple glaciolacustrine units, separated by till

94  and outwash gravel recording at least three glaciations: the last (Late Wisconsinan) glaciation,

95  the penultimate glaciation (Early Wisconsinan), and an earlier glaciation (Ryder et al. 1991;

96  Clague and Evans 2003). The upper part of the sediment sequence was deposited during

97  deglaciation, when repeated glacial lake stages occupied the valley (Fulton 1969; Ryder 1976;

98  Johnsen and Brennand 2004), and shortly after deglaciation when the valley bottom was

99  choked by paraglacial sedimentation (Church and Ryder 1972).

100

101  Modern climate and river discharge, measured respectively 65 km east of Ashcroft at

102  Kamloops and 40 km down Thompson River from Ashcroft near Spences Bridge, reflect

103  seasonally variable weather conditions and hydrology. Precipitation (~250 mm, annual

104  average) is concentrated in May to September (20 mm to 40 mm, monthly) when it falls as

105  rain, and in December and January (20 mm to 30 mm, monthly) when it falls mainly as snow.

106  The driest months are February to April (http://climate.weather.gc.ca/ [2018 URL]). The valley

107  bottom is within the drought-prone Very Dry Hot subzone of the Bunchgrass biogeoclimatic

108  zone (Nicholson et al. 1991; www.for.gov.bc.ca [2018 URL]). Thompson River discharge

109  reflects spring snow melt and rainfall variation. Base flow varies annually from <200 $m^3$/s to

110  ~600 $m^3$/s, with a freshet peak in late May or June of <2,000 $m^3$/s to >4,000 $m^3$/s

111  (http://wateroffice.ec.gc.ca [2018 URL]). The river changes in elevation at Ripley Landslide

112  by over 5 m (264.5 m to 269.8 m elevation) in response to spring melt in the surrounding

113  mountains (Schafer et al. 2015). River levels are at their minimum between early January and

114  early March; and start to rise in late April to early May, continuing through until late July. By

115  early August, river levels are starting to fall.

116

117 *Landslides and their drivers: initial conditions*

118 The presence of steep slopes in bedrock and overlying fill flanking Thompson River is a

119 necessary condition for landslide activity. During deglaciation and early post-glacial (i.e.,

120 paraglacial) time, rapid trunk valley incision in the Interior Plateau, resulting from glacio-

121 eustatic rebound and first time exposure of poorly consolidated sediments, formed over-

122 steepened slopes. Large, retrogressive rotational and translational landslides occurred during

123 the Holocene (Ryder, 1976; Clague and Evans 2003). Although Pleistocene valley fill was

124 preconditioned for failure by rapid incision of unconsolidated glacial units, landslides were

125 most likely triggered by elevated porewater pressure during particularly wet intervals in

126 prehistoric times. Post-glacial climate of the southern Interior Plateau has fluctuated between

127 warmer and cooler than present conditions, but was always generally dry (Hebda 1982;

128 Mathewes and King 1989; Hebda 1995). Even at its wettest, between 6000 and 4000 years ago,

129 climate was not much moister than today (Hebda 1995). Thus, unconsolidated valley-bottom

130 sediments were likely relatively dry through much of the Holocene and remained marginally

131 stable until the 1860s when irrigation, necessary for agriculture on benchlands above the river,

132 began (Stanton 1898; Clague and Evans 2003).

133

134 Historic failure of Pleistocene units involve one of three mechanisms (Porter et al. 2002; Clague

135 and Evans 2003; Eshraghian et al. 2007, 2008): 1) very slow (2 cm/yr to 10 cm/yr) rotational

136 sliding of large, intact blocks; 2) very slow (2 cm/yr to 10 cm/yr) translational sliding of blocks

137 with little rotation; or 3) rapid flow slides and slumps, where fills disaggregate while moving

138 down slope (>2 m/hr). Additionally, extremely rapid (>5 m/s) and very rapid (> 3 m/min) rock

139 falls and debris falls initiate on steep valley walls (cf. Cruden and Varnes 1996), particularly

140 in the Black Canyon. Although many landslides failed rapidly in the past, those that are

141   currently active are very slow-moving, reactivated compound features (Porter et al. 2002;

142   Clague and Evans 2003; Eshraghian et al. 2007, 2008).

143

144   Possible anthropogenic triggers for historical landslides (**Fig. 1** b) include: 1) irrigation of

145   terraces, first by leaky unlined ditches beginning in 1868, and then by confined pipes since the

146   1960s; and 2) excavation of lower slopes during the construction and expansion of rail lines

147   beginning in the 1880s and continuing into this century (Stanton 1898; Clague and Evans 2003;

148   Bunce and Chadwick 2012). Artesian groundwater pressures linked to precipitation further

149   contribute to instability (Porter et al. 2002). Stratigraphy exerts a first order control on the

150   distribution, geometry and rate of landslides along the inner gorge. Most failures occur along

151   weak, sub-horizontal shear zones within glaciolacustrine clay and silt units, confined between

152   overlying till and underlying gravel deposits and bedrock (Porter et al. 2002; Eshraghian et al.

153   2007, 2008; Bishop et al. 2008). Thin, highly plastic clay beds dominate the geomechanical

154   behaviour of the glaciolacustrine units due to their low strength (Porter et al. 2002). The

155   weakest clay zones have residual shear strengths, and were probably previously sheared during

156   glacial overriding and syndepositional landslide events (Porter et al. 2002; Bishop et al. 2008).

157

158   Thompson River influences landslide activity in the inner gorge in several ways. Deep post-

159   glacial incision was first required to expose weak, failure-prone units at the base of the fill

160   sequence and provide kinematic freedom for failure (Porter et al. 2002; Clague and Evans 2003;

161   Eshraghian et al. 2007; Bishop et al. 2008). Ongoing channel migration promotes toe instability

162   (Porter et al. 2002) and alters landslide toe geometry (Eshraghian et al. 2008). Dropping river

163   level exerts a complex control on landslide stability, reflecting increased hydraulic gradients

164   within the basal glaciolacustrine unit, particularly along rupture surfaces within it (Eshraghian

165   et al. 2008), and loss of toe loading (Porter et al. 2002; Eshraghian et al. 2008; Hendry et al.

166  2015). Probably because of several of these effects on toe stabilization, creep commonly

167  accelerates shortly after flood events and during river stage drop following the freshet (Porter

168  et al. 2002; Macciotta et al. 2014; Schafer et al. 2015).

169

170  **Ripley Landslide Test Site**

171  Ripley Landslide is approximately 220 m wide (N-S) by 150 m long (E-W) with an estimated

172  volume of 400,000 m$^3$ (**Fig. 1** c). The landslide has been active since at least 1951, but

173  displacement across the slide body increased after 2005 when a rail siding was constructed

174  across its middle portion (Bunce and Chadwick 2012). During construction, embankments

175  were extended upslope and a lock-block retaining wall, separating the Canadian National

176  Railway (CN) and Canadian Pacific Railway (CP) tracks, was installed (**Fig. 1** d). Pronounced

177  sagging of the retaining wall and bulging of lock blocks has occurred since 2005 (Huntley et

178  al. 2016). To accommodate continual lateral and vertical displacement across the landslide,

179  both rail companies periodically add ballast, in addition to lifting and re-aligning their tracks.

180

181  *Landslide monitoring*

182  Numerous conventional and experimental continuous monitoring technologies (**Fig. 1** c, d)

183  provide insight on the activity, deformation mechanisms, and potential acceleration triggers of

184  Ripley Landslide. Each of these techniques record increased landslide activity in winter, when

185  river and groundwater levels are lowest (Macciotta et al. 2014; Hendry et al. 2015; Schafer et

186  al. 2015; Journault et al. 2018). Four permanent GNSS monuments installed across the

187  landslide in 2008 (**Fig. 1** c) record cumulative annual displacement on the order of 100 mm/yr

188  to 200 mm/yr, which peaks from autumn to winter (Bunce and Chadwick 2012; Macciotta et

189  al. 2014; Hendry et al. 2015). InSAR results from 2013 to 2015 indicate similar magnitudes

190  and spatial-temporal patterns of displacement (Huntley et al. 2017b; Journault et al. 2018).

191  Ground movement concentrated within the centre of the sliding mass averages 39 mm/year,

192  with fastest displacements detected upslope from the railway tracks and on the southern flank.

193  Average and maximum line of sight displacement rates (equivalent to the downslope direction

194  for the west-facing test site) of INSAR corner reflectors (**Fig. 1** c) and other coherent targets

195  (e.g., buildings, large boulders) are 49 mm/year, and 77 mm/year, respectively; with greater

196  displacement from November to March (Huntley et al. 2017b; Journault et al. 2018). Fibre

197  Bragg grating (FBG) and Brillouin optical time domain reflectometry (BOTDR) monitoring of

198  the retaining wall from 2013 to 2015 detected ~ 2 mm of accumulated strain in the wall,

199  including  displacement of individual blocks at its southern end (**Fig. 1** d), with peak activity

200  occurring in the fall and winter months (Huntley et al. 2016; 2017c).

201

202  Subsurface borehole monitoring combining ShapeAccelArray (SAA) inclinometry with

203  piezometer head levels indicate that the main slide body is failing along sub-horizontal, weak,

204  basal shear surfaces in highly plastic clay beds (Macciotta et al. 2014; Hendry et al. 2015;

205  Schafer et al. 2015). The central and northern parts of the slide are translating sub-horizontally

206  (2.1º to 2.5º) whereas the southern portion near the lock-block retaining wall has a steeper (28º)

207  slide surface.

208

209  *Knowledge gaps*

210  Although earth material stratigraphy, textures and penetrative planar structures are important

211  controls on sub-surface porosity, permeability and hydrology in the Thompson River valley

212  (Evans 1984; Porter et al. 2002; Clague and Evans 2003), it remains unclear how these factors

213  influence the style, timing and rate of slope displacement (i.e., form and function) at Ripley

214  Landslide.  Landslide monitoring reveals limited information on the subsurface range of earth

215  materials, structures and hydrological behaviour. A suite of conventional terrain mapping,

216     geophysical methods, field sensors and laboratory techniques were tested in this challenging

217     environment to address significant knowledge gaps in the nature and distribution of surficial

218     earth materials, their stratigraphic relationships and internal structure of the landslide.

219

220     **Methods and Results**

221     Investigations at the Ripley Landslide test site have three aims: 1) characterizing material

222     composition, particularly beneath railway infrastructure; 2) quantifying spatial and temporal

223     characteristics of displacements; and 3) assessing the degree of infrastructure damage. The

224     present study relates principally to the first objective, and provides important context for better

225     addressing the second and third objectives. Landslide form and function in the Thompson River

226     valley are strongly influenced by sub-surface porosity, permeability and hydrology, which are,

227     in turn, influenced by the stratigraphic order of earth materials, textures and penetrative planar

228     structures. To help determine the degree to which these controls influence the nature, extent

229     and activity of Ripley Landslide, we combined terrain mapping, stratigraphic analysis of

230     borehole logs, and several geophysical techniques to characterize hydrogeological variability

231     at the test site.

232

233     *Hydrogeological mapping*

234     Surficial earth materials and landforms were mapped in ArcGIS using ortho-rectified and geo-

235     referenced digital natural colour air photographs taken by a Phantom IV UAV during repeat

236     photogrammetric overflights in September 2016, September 2017 and September 2018. The

237     resulting imagery was sufficient to resolve cobble-sized boulders and anthropogenic features

238     (<5 cm across) at a flight elevation 50 m above ground level. During desktop terrain analysis,

239     visual interpretation of imagery relied on the recognition and separation of geological features

240     using colours, tones, surface textures, patterns, shapes, sizes, shadows and field associations.

241 Fieldwork was undertaken periodically between 2013 and 2019 to ground-truth air photo

242 interpretations, and to describe sedimentological characteristics that could not be determined

243 by remote mapping. With over 80 field stations and 11 boreholes on and adjacent to the

244 landslide, hydrogeological units were defined on the basis of lithofacies and landform

245 associations, texture, sorting, colour, sedimentary structures, degrees of consolidation,

246 stratigraphic contact relationships, geological age, and other distinguishing characteristics

247 described on site (**Fig. 2** a-l). **Fig. 3** depicts the surface and vertical (stratigraphic) distribution

248 of hydrogeological units and landforms at Ripley Landslide and adjacent terrain; more detailed

249 unit descriptions are provided in Huntley and Bobrowsky (2014). Key hydrogeological

250 characteristics of these units are highlighted in **Tab. 1**. Drainage classes and permeabilities were

251 qualitatively determined from field assessments of porosity, unit thicknesses, earth material

252 textures, penetrative planar structures and slopes driving hydraulic gradients (**Tab. 1**).

253 <u>Observations of textures and porosity variations in hydrogeological units</u>

254 Pleistocene and Holocene sediments unconformably overlie fine-grained, massive crystalline

255 andesite (unit 1a, **Fig. 2** a) and fine-grained, flow-banded crystalline rhyolite (unit 1b) with low

256 or negligible intercrystalline porosity, and welded clast-supported agglomerates with a low

257 vugular porosity (**Fig. 2** b; **Tab. 1**). The oldest Pleistocene deposits (unit 2) are up to 6 m thick

258 and include intercalated centimetre-thick beds of clay, silt, sand, gravel and diamicton (**Fig. 3**)

259 with moderate intergranular porosity. This basal unit is disconformably overlain by up to 12 m

260 of silt-clay couplets (i.e., varves) with dropstones and stratified diamicton with low

261 intergranular porosities (**Fig. 2** c, d). Units 2 and 3 are glaciolacustrine in origin and were

262 deposited during the retreat phase of a penultimate glaciation and advance of the Late

263 Wisconsinan Cordilleran Ice Sheet, respectively. Glaciolacustrine units are over-consolidated,

264 deformed, eroded and overlain by unit 4, a massive, matrix-supported diamicton up to 5 m

265 thick composed of silt, clay, erratic boulders and ice-rafted blocks of locally derived bedrock,

266    interpreted as a (subglacial) lodgement till (**Fig. 2** e). Consolidation of unit 3 causes silt and

267    clay particles to densely pack, resulting in an increase of effective stress, combined with a

268    decrease in void ratio, water content, and permeability (Le Meil 2017).  The permeability of

269    glaciolacustrine units is anisotropic, with horizontal permeability (along the rhythmite beds)

270    an order of magnitude larger than the vertical permeability (across beds). Heterogeneities

271    caused by fissures and sand laminae intersecting the glaciolacustrine silt and clay significantly

272    enhance the bulk permeability of units 2 and 3. Till has a low vugular porosity due to the

273    presence of isolated weathered igneous and sedimentary clasts and sand-filled voids within the

274    fine-grained matrix. Field observations, borehole logs and geophysical data all indicate that

275    unit 4 till contains ice-rafted bedrock blocks. Silt-rich glaciolacustrine sediments (unit 5, **Fig.**

276    **2** f), containing centimetre-thick sand beds with moderate intergranular porosity, conformably

277    overlies till. During summer months, salt crusts form where solute-rich groundwater seeps and

278    evaporates from exposed sand-rich beds in units 3 and 5 along railway embankments and river

279    cutbanks. Above unit 5 lies >5 m of massive and crudely stratified beds of open framework,

280    clast-supported boulder and sand-rich gravel (unit 6, **Fig. 2** g). This coarse-grained

281    glaciofluvial unit has a high intergranular porosity.

282

283    The oldest Holocene deposits, unit 7 (**Fig. 2** h), consist of interbedded stratified diamicton and

284    open framework, clast-supported cobble-gravel incised into unit 6. This basal sequence fines

285    upward to massive centimetre-thick sand and silt beds with moderate intergranular porosity.

286    Bedding lies sub-parallel to surface slopes ranging from >3$^o$ to <8$^o$ on alluvial fans, and >8$^o$ to

287    <12$^o$ on alluvial cones. Slopes >12$^o$ are covered in postglacial coarse-grained colluvium with

288    a high intergranular porosity (unit 8, **Fig. 2** i). Moderate slopes from >12$^o$ to <26$^o$ are covered

289    in a veneer of stratified diamicton and clast-supported cobbles, boulders with interstitial sand

290    and silt. Moderately steep bedrock slopes from >26$^o$ to <35$^o$ are covered in a veneer of clast-

291 supported talus blocks. Modern alluvial floodplain sediments (unit 9, **Fig. 2** j) are open

292 framework, clast-supported boulders and sand with a high intergranular porosity, confined to

293 elevations lower than 270 m. Surface water is quickly removed during heavy or prolonged

294 rainfall, and boulders and sand are permanently saturated by river water at shallow depth ($<$2

295 m) on the active flood plain. Bedrock, glacial and alluvial sediments (units 1-5 and 9),

296 excavated during track construction, are unconformably overlain by a linear deposit ($<$5 m

297 thick) of open framework, clast-supported cobble and boulder ballast and a lock-block retaining

298 wall (unit 10) with high intergranular porosity (**Fig. 2** k, l).

299

300 <u>Penetrative structures observed in hydrogeological units</u>

301 Unit 1 has moderate fracture porosity (**Tab. 1**). Fine-grained crystalline andesite (unit 1a) has

302 two dominant sets of vertical joints, trending W and NW; overlying rhyolite and volcaniclastic

303 rocks (unit 1b) have vertical fractures trending NW and SW. Volcaniclastic rocks dip eastward

304 into the slope. These penetrative features are an expression of the regional folding and faulting

305 history. Surface weathering rinds and mineral alteration are observed along exposed surfaces,

306 including open fractures. Surface exposures and borehole logs reveal overlying

307 glaciolacustrine units 2 and 3 have low to moderate fracture porosities with discrete zones

308 where clay-rich beds are intensely cracked, fissured and sheared (**Fig. 3**). Sub-till silt and clay

309 beds with contorted layering and loading structures indicate deformation during the overriding

310 of glacial lake deposits by ice during the last glaciation (**Fig. 2** c, d, e). Cross-cutting (and

311 younger) penetrative structures are observed at depths between 5 m and 15 m below surface,

312 confined to unit 3. Below 270 m elevation. sub-horizontal planar surfaces dip from 5º to 30º

313 W toward and underneath the river (**Fig. 3**, **Tab. 1**). These structures are interpreted as

314 translational-rotational shear planes related to current landslide movement. Slide scarps,

315 crescentic tension cracks on the slide body and surface relaxation (unloading) fractures along

316    railway embankments are sub-vertical, penetrate deep into the slide body (greater than 2 m

317    depth) and cross-cut multiple units (**Fig. 2** e, f). These penetrative structures impart a moderate

318    to high fracture porosity in till diamicton (unit 4), silt-rich glaciolacustrine beds (unit 5),

319    postglacial alluvium (unit 7), colluvial sediments (unit 8), and anthropogenic materials (unit

320    10). Coarse-grained glaciofluvial deposits (unit 6) and modern alluvial floodplain sediments

321    (unit 9) have no penetrative planar structures (**Tab. 1**).

322

323    *Geophysical field mapping*

324    The objective of the geophysical surveys was to measure contrasts in the physical properties of

325    unconsolidated sediments and bedrock, interpreted in the context of the known lithological units

326    on site (Huntley and Bobrowsky 2014; Huntley et al. 2017a, b). Geophysical surveys were

327    undertaken between 2013 and 2015 using a combination of terrestrial and waterborne electrical

328    resistivity tomography (ERT), frequency domain electromagnetic conductivity measurements

329    (FEM), ground penetrating radar (GPR), seismic primary wave refraction (PWR) and

330    multichannel analysis of surface waves (MASW); in conjunction with down-hole measurement

331    of natural gamma radiation (GR), induction conductivity (IC) and magnetic susceptibility (MS)

332    in boreholes located directly adjacent to the CPR tracks (**Fig. 3**; **Tab. 2**). Geophysical traverses

333    were spaced across the breadth of the landslide and Thompson River to ensure reasonable

334    diversity in coverage of the subsurface variability (**Fig. 4**). Terrestrial cross-sections extended

335    from behind the landslide head scarp to the channel bank (November 2013). River survey lines

336    trended parallel to the shoreline (November 2014), and were traversed using a metal-hulled jet

337    boat towing a non-metallic white-water raft containing the geophysical equipment. With regard

338    to geoelectrical properties, five terrestrial ERT lines used a Wenner-Schlumberger array with

339    48 electrodes spaced 5 m apart. Four waterborne ERT lines used a reverse Wenner array with

340    an electrode spacing of 10 m (Huntley et al. 2017a; Huntley et al. 2019a). Apparent resistivity

341    datasets were merged into a single file and interverted using the RES3DINV inversion program

342    (geotomosoft.com 2017; Huntley et al. 2019b).

343

344    A Proactive Infrastructure Monitoring and Evaluation (PRIME) resistivity monitoring system

345    was installed on the Ripley Landslide in November 2017 (Holmes et al. 2018). This system,

346    which provides near-real time 4-D resistivity data, consists of two intersecting Wenner arrays

347    (one 91 m long with 45 electrodes, the other 54 m long with 27 electrodes, all evenly spaced).

348    The PRIME system is connected to the internet via a modem and allows for remote data

349    acquisition. When calibrated with soil moisture measurements and laboratory testing of earth

350    materials, continuous data collection allowed for changes in subsurface condition to be

351    monitored over time (cf. Merritt et al. 2014; Uhlemann et al. 2017), and improves understanding

352    of seasonal changes in the hydrogeological regime of the landslide (Huntley et al. 2019c).

353

354    *Soil moisture monitoring*

355    The importance of soil suctions (negative pore water pressure) on slope instability has long

356    been recognized (Fredlund et al. 1976). Soil suctions increase the strength of soil and help

357    stabilize slopes. However, transient near-surface changes in suction pressures, as a result of

358    climatic conditions, may be sufficient to induce slope movement. In November 2017, two

359    Decagon MPS6 soil suction meters were installed in the headscarp of Ripley Landslide to a

360    depth of 2 m (Sattler et a. 2018); another three experimental meters were placed in November

361    (**Fig. 4**). The potential use of resistivity as a proxy for suction has been previously suggested

362    (Piegari and Di Maio 2013). In the coming years, the relationship between these parameters

363    will be investigated using preliminary PRIME and soil suction sensor data from unit 3.

364

365    ERT results and hydrogeological units

366    An unprecedented level of insight into the internal composition and structure of the landslide

367    has been gained from the terrestrial, waterborne and borehole geophysical surveys (**Tab. 2**).

368    The ERT surveys provide the most complete and deepest penetrating information regarding the

369    internal structure of the landslide (Huntley et al. 2017a, b; Huntley et al. 2019a, b). The FEM

370    only images the upper 10 m, but results are consistent with ERT data, and add additional useful

371    information on the near surface resistivity/conductivity distribution (Huntley et al. 2017a, b;

372    Huntley et al. 2019a, b). Seismic surveys provide information on earth material stiffness at

373    depth. GPR data show interesting results (Huntley et al. 2017a), but there are difficulties in

374    interpretation due to the predominance of clay-rich sediments, and numberous diffracting

375    centres, mostly boulders at various depths (**Tab. 2**).

376

377    The terrestrial-based ERT survey undertaken in November 2013 and waterbourne ERT survey

378    completed in November 2014 are presented with PRIME data from November 2018 in a fence

379    diagram showing the range of electrical properties of the landslide (**Fig. 5**). Since the surveys

380    were completed at the same time of year, differences arising due to the influence of seasonal

381    changes in weather conditions on the electrical properties were minimised by selecting

382    November as the month of observation, and ensures that the electrical properties are

383    comparable, although completed in different years. Data from the terrestrial-based ERT lines

384    were inverted in 3D using Res3DInv (geotomosoft.com 2017), taking account of the offline

385    variation in topography in the topographically complex area of the slide. This improved the

386    correlation between each of the lines, reducing the mismatch in resistivity values at depth. The

387    waterbourne survey data were inverted in 2D using Res2DInv (geotomosoft.com 2017). The

388    lines are displayed in ParaView® alongside the PRIME ERT lines (**Fig. 5**).

389

390    Combined terrestrial and waterborne 2D ERT datasets are visualized as a pseudo-3D model of

391    resistivity values using ParaView® software (**Fig. 6**). Competent bedrock (unit 1) has a high

392    apparent resistivity value, >110 Ωm (**Fig. 6**). Weathered bedrock and colluviated fine-grained

393    beds at the base of unit 2 are moderately resistive (80 Ωm to 110 Ωm). Overlying  areas with

394    low resistivity values (<80 Ωm) are correlated with the oldest Pleistocene glaciolacustrine

395    sediments, units 2 and 3 (**Fig. 6**). Unit 4 lodgement till appears as a moderately resistive (80

396    Ωm to 110 Ωm) silt, clay and boulder diamicton up to 5 m thick (**Fig. 2** e). Silt-rich

397    glaciolacustrine sediments (unit 5, **Fig. 2** f) have low resistivity values (<80 Ωm). Overlying

398    glaciofluvial outwash (units 6 and 7, **Fig. 2** g) are moderately resistive (80 Ωm to 110 Ωm)

399    when undersaturated (dry). Coarse, rapidly drained colluvium (unit 8) has a high apparent

400    resistivity value >110 Ωm (**Fig. 6**). Modern alluvial floodplain sediments (unit 9, **Fig. 2** j) are

401    saturated (wet) through much of the year and return high apparent resistivity values (**Fig. 6**).

402    Coarse ballast (unit 10), when undersaturated (dry), has a high apparent resistivity >110 Ωm

403    (**Fig. 6**).

404

405    The PRIME system has provided new insight into the hydrogeological structure of the slope

406    (**Fig. 7**). The ERT models reveal a complex stratigraphy of coarse colluvial sediments (unit 8)

407    overlying massive silt-rich diamicton (unit 4) with tension cracks over 0.5 m wide and 1 m

408    deep, and highly fissured laminated silts and clays (unit 3) in which the landslide failure plane

409    lies. Large decreases in surface resistivity (>50%) by through (March to May) are due to an

410    increase in moisture content are due to snowmelt and intense, short-duration precipitation

411    events. Temperatures are consistently above 0°C by this time, and despite a negative weekly

412    effective rainfall during this season, the additional moisture resulting from snowmelt is

413    sufficient to increase the moisture content of the slope. This demonstrates the need for

414    subsurface imaging in such locations where both temperature and precipitation control

415  groundwater hydrology, as this hydrogeological regime could not be predicted from weather

416  data alone. In addition, the spatial variations in resistivity changes are also revealed, which

417  again highlights the need for subsurface investigation. The propagation of the wetting front

418  along the failure plane  is clearly shown in **Fig. 7**, indicating that the headscarp acts as a major

419  conduit for the flow of groundwater. Long-term monitoring of the slope will provide an insight

420  into the seasonal variations in subsurface moisture, and combining this with near-real time

421  displacement data will enable a long-term goal of developing moisture thresholds for failure to

422  be realized.

423

424  Borehole geophysics results and hydrogeological units

425  Downhole natural GR levels, IC and MS surveys of boreholes BH15-01, BH15-02 and BH15-

426  03 (**Fig. 3** and **Fig. 5**) provide further insight into the sub-surface thickness of earth materials,

427  depth to bedrock, groundwater conditions and failure mechanisms of the landslide. East of the

428  CPR tracks, the Mount Sopris MGX logging tool encountered 15 m to 17 m of glacial deposits

429  overlying basal bedrock in the boreholes (**Fig. 5**). West of the CN tracks, boreholes show around

430  30 m of till and clay-rich glaciolacustrine sediments overlying bedrock (**Fig. 3** and **Fig. 5**).

431  These observations corroborate the terrestrial and waterborne geophysics results indicating the

432  main landslide body is located over a >20 m deep bedrock basin underlying the modern

433  Thompson River.

434

435  Natural GR logs show a relatively constant response (**Fig. 3** and **Fig. 5**), interpreted to indicate

436  the predominance of clays in the glacial deposits. Minor changes in readings throughout the

437  borehole reflect small variations in sand, clay and silt content, and levels of Uranium, Thorium

438  and Potassium in granitic and arkosic dropstones (units 2 and 3) and erratics (in unit 4) directly

439  adjacent to boreholes. The IC logs show an initial progressive, but subtle rise in conductivity

440  values (**Fig. 3** and **Fig. 5**) corresponding to an increase in clay content with depth. High

441  conductivity zones may indicate clay horizons in silt- and boulder-rich till (unit 4). At depth,

442  conductivity levels fall in response to a lower clay content at depth (unit 3), decreasing porosity

443  in stiff to hard silt-clay diamicton (unit 2), and electrically resistive andesite intersected in the

444  bottom of boreholes (unit 1). The MS logs show a consistently low response (**Fig. 3** and **Fig.**

445  **5**) indicating a very low ferromagnetic mineral content in the surrounding glacial deposits

446  (units 2 to 5). The slight decrease in MS apparent near the base of each borehole corresponds

447  to the intersection of unconsolidated glacial deposits with andesite bedrock (**Tab. 2**).

448

449  <u>Pertrophysical property relationships from sensor data</u>

450  Petrophysical property relationships of the materials comprising the landslide complement and

451  provide improved understanding and interpretation of field resistivity measurements. Field

452  suction-resistivity relationships have been estabilished by relating the resistivity of the head

453  scarp as revealed by the PRIME data with sensor data from the head scarp (**Fig. 8**). The daily

454  average suction is plotted alongside the daily average resistivity of the cells in the resistivity

455  model corresponding with the suction sensor location and depth. The location of the suction

456  sensor is shown in **Fig. 4**. Resitivity increases as suction increases. This relationship is

457  expected, as both suction and resistivity are known to increase as moisture content decreases.

458  A deviation from this trend is observed mid-January when daily resisitvity was higher than

459  expected. This is likely due to localized freezing at the surface which results in increased

460  resistivity. This is supported by the weather data, which shows temperatures below $0^{\circ}$C around

461  this time. Therefore, there is an increase in resistivity despite the fact that effective rainfall was

462  positive during this period, which is usually associated with decreased resistivity.

463

464 Future work will build upon these relationships, and focus on laboratory investigations of the

465 three different hydrogeological units present in Ripley Landslide (unit 3 - silt and clay; unit 4

466 - till diamicton; unit 8 – colluvial diamicton). The work will focus on the development of

467 resistivity-moisture content, suction-moisture content, and resistivity-suction relationships for

468 samples taken from each unit. Given the importance of temperature at this site, laboratory

469 experiments will be carried out under a range of conditions, using temperatures recorded onsite

470 as a basis for experimental design.

471

472 **Discussion: Hydrogeological and Geophysical Properties of Ripley Landslide**

473 Lying within the semi-arid Bunchgrass biogeoclimatic zone, slope stability at Ripley Landslide

474 is strongly influenced by local geological properties, hydrological conditions and channel

475 morphology. For much of the Holocene, infiltration of snow melt, precipitation and surface

476 runoff was very limited: generally, winters and springs are dry, and summer heat causes rapid

477 evaporation of precipitation (cf. Nicholson et al. 1991). Pleistocene and Holocene valley fill

478 was destabilized after irrigation of benchlands began in the 1860s, and inner canyon toe slopes

479 were excavated in the 1880s, 1950s and 2000s to accommodate CN and CPR tracks (Clague

480 and Evans 2003; Bunce and Chadwick 2012). Surficial mapping, borehole logs, and

481 geophysical surveys indicate the main landslide mass comprises a >20 m thick package of

482 Pleistocene and Holocene sediments, unconformably overlying bedrock, that extends from

483 under Thompson River to approximately 280 m elevation (**Fig. 5** and **Fig. 6**). Permeability,

484 porosity and drainage of bedrock and surficial units in the landslide are strongly influenced by

485 bed thicknesses, earth material textures, penetrative planar structures and slopes driving

486 hydraulic gradients. These properties constrain the interpretation of geophysical results (**Tab.**

487 **2**) and modelling of landslide form and function.

488

*Drainage characteristics of hydrogeological units*

At the surface, electrically resistive andesite (unit 1a), rhyolite and volcaniclastic rocks (unit 1b) are relatively well-drained where moderately permeable shallow bedrock fractures and bedding planes allow downward percolation of water (**Tab. 1**). At depths >2 m, and elevations lower than 270 m (i.e., below river level), bedrock fractures with low permeability are poorly drained and remain saturated during high river stage (e.g., in spring and summer) or sealed.

More than 20 m of Pleistocene and Holocene sediment unconformably overlies unit 1 bedrock (**Fig. 3**). Locally fractured and bedded sediments of unit 2 are imperfectly drained. Below 270 m elevation, coarser sediments remain saturated for much of year, especially during higher river stages. Unit 3 is poorly drained in the sub-surface, with fine-grained sediments remaining undersaturated for much of year. The exception would be during prolonged rainfall, snow melt, sustained confined groundwater flow and high river stage. Unit 4 diamicton and clay-rich glaciolacustrine beds of unit 5 are imperfectly drained, with fractures allowing downward infiltration of surface water and subsurface flow of groundwater. Both units become saturated at depth during prolonged rainfall, snow melt and at high river stage (**Tab. 1**). At depth, vertical fractures and sub-horizontal planes become saturated during prolonged rainfall or snow melt.

Upslope of the landslide, highly permeable coarse-grained glaciofluvial sediments (unit 6) are rapidly drained. Percolating surface water and groundwater is quickly removed downslope, with subsurface flow during heavy or prolonged rainfall, and snow melt indicated by the ERT data (Huntley et al. 2019b). Moderately permeable unit 7 alluvial diamicton, silt and sand deposits are well drained, and during snow melt and heavy or prolonged rainfall, percolating water is readily removed downslope by subsurface seepage (**Tab. 1**). Highly permeable coarse-grained colluvial sediments (unit 8), alluvial floodplain deposits (unit 9), ballast, lock-block

514    retaining walls and metal culverts (unit 10) are rapidly drained, with percolating surface water

515    and groundwater quickly removed downslope, and subsurface flow occurring during heavy or

516    prolonged rainfall and snow melt (**Tab. 1**).

517

518    *Geophysical model of hydrogeological units*

519    Pseudo-3D models capture resistivity, soil moisture and groundwater conditions in surficial

520    deposits and bedrock for the fall seasons of 2013 and 2014 (**Fig. 5** and **Fig. 6**). This

521    representation is interpretation-oriented, with the selection of resistivity thresholds at 80 Ωm

522    and 110 Ωm determined by observations of earth materials, and their hydrogeological properties

523    at surface and in logged boreholes (**Fig. 2** and **Fig. 3**). Electrically resistive earth materials

524    (>110 Ωm, red on **Fig. 6**) include undersaturated (dry) sand and gravel (unit 6), till diamicton

525    (unit 4) and competent bedrock (unit 1). Bedrock, clay, till and gravel saturated with

526    groundwater are all conductive bodies (<80 Ωm, blue on **Fig. 6**). Along the north and south

527    boundaries, a transition from bedrock to saturated clay-rich glacial sediments beneath the river

528    is recorded between 220 m and 240 m elevation by a drop in resistivity values to below 80 Ωm.

529    From 240 m to 270 m elevation, conductive earth materials (<80 Ωm) are bounded by resistive

530    zones (>110 Ωm) beneath the river and east valley slope (**Fig. 6**). This pattern is interpreted to

531    represent a north-south oriented bedrock palaeochannel fragment infilled with remobilized

532    glacial deposits (units 2 and 3). The 2D waterborne ERT dataset (Huntley et al. 2017a; Huntley

533    et al. 2019a) and pseudo-3D model (**Fig. 6**) show a significant portion of the landslide lying

534    below river level from approximately 270 m to 230 m elevation. The main slide body is

535    represented as an ovate conductive zone (<80 Ωm) containing inliers of resistive material (>110

536    Ωm) along the northern, eastern and southern flanks (**Fig. 6**). These latter features are

537    interpreted as locally derived bedrock blocks remobilized during glaciation.

538

539    Conductive zones logged in the boreholes (Huntley et al. 2017a) suggest an increase in water

540    content along tension cracks, fissures, fractures and shear planes within clay, silt- and boulder-

541    rich till (unit 4) at around 5 m depth (**Fig. 3**). Deeper fissures recorded in the borehole logs and

542    field observations are not represented in the conductivity readings, suggesting lower water

543    content at these depths. Strong reflectors in GPR profiles (Huntley et al. 2017a) may also

544    represent saturated clay, silt (units 3 and 5), coarser diamictons (units 2 and 4), and bedrock

545    (unit 1) at depths < 20 m (**Tab. 2**). Higher conductivity (i.e., low resistivity, <80 Ωm) values

546    in units 2, 3 and 4 beneath the Thompson River detected by waterborne ERT (**Tab. 2**) may be

547    attributed changes in clay and groundwater content of sub-river units. Three zones of elevated

548    terrain conductivity across the submerged landslide toe have been identified in the bathymetry-

549    corrected waterborne FEM data (**Fig. 6**), These zones are interpreted to indicate areas where

550    artesian groundwater in units 2, 3 and 4 is discharging through the boulder lag (unit 9) covering

551    the river bed (Huntley et al. 2017a; Huntley et al. 2019a).

552

553    Upslope of the river floodplain and railway ballast, at elevations from 270 m to 295 m,

554    resistivity values >110 Ωm are intersected. This range in values is consistent with unsaturated

555    silt, sand and cobble colluvium overlying bedrock (**Fig. 6**). The distribution of these units

556    suggests a 290 m elevation limit to eastward headscarp retrogression and potential maximum

557    volume of approximately $0.8 \times 10^6$ m$^3$ for the landslide. Above the head scarp, zones of higher

558    conductivity occur where soil water is migrating toward the water table through silt, sand and

559    cobbles exposed by hill slope erosion (**Fig. 6**). Upslope of the landslide, zones of high resistivity

560    (>80 Ωm) in units 5, 6 and 7 occur where soil water is migrating toward the water table through

561    silt, sand and cobbles exposed by gully erosion (**Tab. 2**; **Fig. 5**).

562

563    *Landslide function: observations of hydrogeology and geophysical data*

564 Fluctuations in stream discharge and river level affect the stability of Ripley Landslide in three

565 ways: 1) by changing the porewater pressure on the rupture surfaces in units 2, 3 and 4; 2) by

566 changing the loading pressure on the submerged toe slope; and 3) by altering the slide geometry

567 through cutbank erosion, channel incision and toe scour. An increase in slope instability occurs

568 during years when the river level is elevated above average for longer than normal periods.

569 During spring run-off, high water levels provides temporary loading support at the landslide

570 toe, resulting in slower movement rates. Higher ground movement rates occur during autumn

571 and winter when river discharge and groundwater levels drop, reducing load values on the slide

572 toe and porewater pressures in the main body (cf. Eshraghian et al. 2007; Hendry et al. 2015;

573 Journault et al. 2018).

574

575 Elsewhere in the Thompson River valley, failing glaciolacustrine beds are highly plastic, with

576 plastic/liquid limits ranging from 45% to 90% and residual friction angles of $10^{o}$ to $15^{o}$ (Schafer

577 et sl. 2015; Le Meil 2017). Silt beds in units 2, 3 and 5 have higher overall residual shear

578 strength compared to clay beds, with values ranging from $>26^{o}$ to $<35^{o}$ (cf. glacial pond to

579 steep-dipping silt-rich debris flow diamictons draped over bedrock in **Fig. 2** c). At Ripley

580 Landslide, field observations and borehole logs show that deformation and erosion by glaciers

581 or pre-historic slope movement have created pre-sheared discontinuities in units 2, 3 and 4 (**Fig.**

582 **2** d) at a residual strength that predispose these sediments to failure (cf. Clague and Evans 2003;

583 Eshraghian et al. 2007; 2008). Fine-grained glacial sediments (units 2 to 4) have low

584 permeability (**Tab. 1**) and exhibit subtle resistivity changes reflecting variations in total clay

585 and groundwater content across the slide body (**Fig. 6**).

586

587 Seasonal wetting and softening of clay beds may contribute to slope failure (cf. Clague and

588 Evans 2003). Surface and borehole monitoring indicate that much of the landslide moves very

589 slowly (cumulatively <55 mm/yr) on gentle (<2°) channel-sloping failure planes developed in

590 weak, highly plastic layers of fine-grained glaciolacustrine silt and clay (**Fig. 3**). Failure of units

591 2 to 5 occurs as shear strength is reduced in response to periods of saturation when the residual

592 friction angle of clay layers falls below the angle of slope (generally <25°). The ERT data show

593 that these failing sediments are conductive (<80 Ωm), potentially saturated with groundwater,

594 and extend under the river (**Fig. 6**). Sediments of units 2 to 5 readily move, even on gentle

595 slopes, due to a reduction in shear strength with increasing saturation of sediments and

596 penetrative structures. All other surficial units contain little clay, are non-plastic and permeable

597 to some degree. The presence of penetrative structures (e.g., tension cracks and slide surfaces),

598 bedding thickness and porewater pressure in sand and gravel beds within glaciolacustrine units

599 influence the effective stress condition of the slope (cf. Clague and Evans 2003; Bishop et al.

600 2008). The residual friction angle of clay beds in glaciolacustrine units is stress dependant: high

601 normal stresses promote alignment of clay particles during shear (Schafer et al. 2015; Le Meil

602 2017). Greater normal stresses beneath the main body of the landslide are expected where

603 InSAR and GNSS measurements show rates of movement are highest, and where geophysical

604 data indicate surficial deposits are >20 m thick. While the rate of movement is very slow, rapid

605 failure is possible under certain conditions. For example, when surface tension cracks fill with

606 infiltrating water (or snow) and landslide debris becomes saturated by rising river and

607 groundwater levels.

608

609 Waterborne geophysical surveys reveal that the landslide extends under Thompson River,

610 where sediments are generally <20 m thick and river levels vary seasonally by >2 m. Fine-

611 grained beds (units 3 and 4) in the submerged toe are armoured from erosion by a lag deposit

612 of modern fluvial boulders (unit 9) except where a deep trough and scour pool is carved by

613 strong currents (**Fig. 4**). Here, bedding and sliding surfaces are exposed at the bottom or slightly

614    below the riverbed (<270 m elevation). For the submerged toe, shear rates are likely to be lower,

615    variable and stage-dependent (cf. Porter et al. 2002; Schafer et al. 2016). Scour holes and

616    cutbank erosion are evidence that the river continues to incise the channel floor (**Fig. 4**) when

617    rock fall debris (unit 8) constricts stream flow, locally increasing current velocity. Higher rates

618    of landslide movement might be triggered along deep-seated rupture planes if plastic clay beds

619    near the top of unit 3 (seen in borehole logs, e.g., **Fig. 6**) become exposed during channel

620    incision. Cutbank erosion is also producing over-steepened toe blocks along the main channel.

621    If these blocks fail and are removed when river and groundwater levels are low, toe slope

622    unloading may contribute to rapid movement on rupture surfaces (cf. Eshraghian et al. 2007).

623    Toe slope incision is occurring adjacent to where the highest ground motion rates are recorded

624    on the landslide (Macciotta et al. 2015; Hendry et al. 2015; Journault et al. 2018). This is also

625    where critical railway infrastructure is at risk (i.e., the lock-block retaining wall and tracks; **Fig.**

626    **1** d). The seasonal addition of ballast, combined with longer, heavier and more frequent trains

627    crossing the main slide body may also contribute to subaerial loading. It is not known whether

628    these factors trigger increased movement during times of reduced shear strength.

629

630    Lastly, extreme weather events and climate change have the potential to exacerbate ongoing

631    landslide activity at the test site. Although the average rainfall in the area has increased since

632    the 1920s, there is no direct correlation with landslide activity (Porter et al. 2002; Eshraghian

633    et al. 2007). However, increased duration and magnitude of precipitation, loss of vegetation

634    cover, reduced soil cohesion by wildfires and fluctuating river discharge could contribute to

635    sustained periods of groundwater recharge, increased porewater pressures in bedrock and

636    surficial units, higher seasonal river discharges and greater channel erosion triggering additional

637    landslide activity in the Thompson River valley. Irrigation water does not directly contribute to

638    instability of Ripley Landslide since the surrounding slopes are still used as rangeland.

639 However, grazing limits the already sparse vegetation cover and cattle trails form intermittent

640 linear paths of disturbed soil forming narrow slope breaks that contour slopes. These conditions

641 contribute to infiltration of precipitation, snow melt and surface runoff into the unconsolidated

642 valley fill.

643

644 **Summary and Conclusions**

645 The overarching goal of our work is the mitigation of risks to public safety, the environment,

646 and railway transportation infrastructure. Studies of Ripley Landslide provide important insight

647 into processes and behaviour of similar, but much larger, landslides between Ashcroft and

648 Basque Ranch (**Fig. 1**). Like others landslides in the Thompson River valley (Porter et al. 2002;

649 Clague and Evans 2003; Eshraghian et al. 2007), seasonal movement occurs along sub-

650 horizontal translational rupture surfaces corresponding to weak glacially sheared zones in

651 glaciolacustrine clay and silt (unit 3) and till (unit 4) (**Fig. 3** and **Fig. 5**). This constant activity

652 has the potential to cause damage to railway tracks and disruption of service with risks to the

653 national economy, the local environment, and natural resources (e.g., potable water and

654 salmon).

655

656 Significant gaps in the knowledge of the nature of bedrock and surficial earth materials, their

657 stratigraphic relationships; and in the controls on the style of mass wasting have been addressed

658 here. By combining terrain analysis and modelling of multidimensional geophysical datasets,

659 we have revealed an unprecedented level of detail in the internal composition, structure and

660 hydrology of the very slow-moving Ripley Landslide. This paper helps to explain how

661 hydrogeological conditions influence the spatial and temporal patterns of surface water and

662 groundwater flow; and how future changes in climate and landscape conditions might influence

663 landslide activity along Thompson River.

664

665     At the test site, >20 m of glacial deposits with contrasting porosity and permeability are

666     preserved in a fractured bedrock paleo-channel basin. Bedrock and unconsolidated sediments

667     have been subaerially exposed by post-glacial valley incision, and during construction of the

668     railway corridor since the late $19^{th}$ century. The pool and riffle channel morphology of

669     Thompson River at Ripley Landslide is significant because hydraulic conductivity between the

670     river, landslides and groundwater systems likely increases where fractured bedrock and

671     glaciolacustrine units (containing impermeable silt-clay couplets, coarse porous beds, lateral

672     failure planes and vertical tension cracks) are continually exposed by fluvial erosion. Scour

673     pools are also identified adjacent to irrigated benchlands along the study reach. These terraces

674     are potentially unstable and should be monitored together with active landslides for surface

675     subsidence, tension cracks and scarps to better manage geohazard risks in the Thompson River

676     valley.

677

678     Field observations (**Tab. 1**) and geophysical data (**Tab. 2**) indicate that Pleistocene units 4 to

679     7 host an unconfined aquifer recharged by infiltrating precipitation and surface runoff across

680     Ripley Landslide, and from the slopes above. Soil water and groundwater flow laterally and

681     downward through porous till and glaciofluvial sediments (units 4 and 6), and through

682     vertically fractured glaciolacustrine units (3 and 5), until it encounters fractured, non-porous

683     bedrock (unit 1) or sub-horizontal shear zones in unit 3. As with other landslides in the area,

684     units 2, 3 and 5 function as aquitards, but also accommodate landslide movement and porewater

685     migration along shear zones approximately corresponding to stratigraphic boundaries (**Fig. 5**).

686     Artesian conditions at the landslide toe suggest the presence of an aquifer in unit 1 (bedrock)

687     and unit 2 (diamicton), confined by clay and silt layers in units 2 and 3 (cf. Macciotta et al.

688     2014; Hendry et al. 2015; Schafer et al. 2015). Recharge sources include groundwater flow

through buried paleochannels and along unconformities separating older glacial sequences (cf.

Porter et al. 2002; Clague and Evans 2003). This confined aquifer controls porewater pressures

at the base of unit 3.


A continuous (real-time) proactive infrastructure monitoring and evaluation (PRIME) system

has now been deployed to characterize the long-term hydrological behaviour of the landslide

by monitoring dynamic (pseudo-4D) changes in electrical resistivity (cf. Merritt et al. 2014;

Uhlemann et al. 2017; Huntley et al. 2019b). To establish the petrophysical relationship linking

resistivity to moisture content, laboratory testing of three samples (units 3, 4 and 8), collected

across the landslide, was undertaken at the British Geological Survey facilities at Keyworth,

UK. A continuous dataset will help to better define: 1) contributions from surface runoff,

precipitation, freeze-thaw cycles, and snow melt to seasonal variations in slope movement; 2)

surface water and groundwater flow paths through the main slide body, the river and bedrock;

and 3) the relationship of fluctuating porewater pressures monitored in boreholes and landslide

activity. Relationships between suction and resistivity derived from field data (Holmes et al.

2018; Sattler et al. 2018) demonstrate the importance of changing moisture content (and

therefore changing suction and pore pressures) for resistivity, but given the wide range of

geological units present on the site, understanding the hydrogeological properties of each unit

will be pivotal in providing improved understanding of slope stability in the Thompson River

valley.  As such, future work will focus on the laboratory testing of samples from different

units of the Ripley landslide, building upon relationships identified in the field to establish

relationships between moisture content, suction and resistivity. These relationships will then

be used to better constrain the inversion of the ERT data. This new understanding will guide

the interpretation of multi-year monitoring datasets (e.g., GNSS, InSAR) and future efforts to

track landslide activity in the Thompson River valley.

731

732 **References**

733 Beatty, T.W., Orchard, M.J., and Mustard, P.S. 2006. Geology and tectonic history of the

734 Quesnel terrane in the area of Kamloops, British Columbia. *In* Paleozoic evolution and

735 metallogeny of pericratonic terranes at the ancient pacific margin of North America,

736 Canadian and Alaskan Cordillera. Geological Association of Canada, Special Paper, **45**: 483-

737 504

738

739 Bishop, N., Evans, S., Petley, D., and Unger, A. 2008. The geotechnics of glaciolacustrine

740 sediments and associated landslides near Ashcroft (British Columbia) and the Grand Coulee

741 Dam (Washington). *In* From Causes to Management. 4th Proceedings of the Canadian

742 Conference on Geohazards, 594 p

743

744 Bobrowsky P., Sladen W., Huntley, D., Zhang, Q., Bunce, C., Edwards, T., Hendry, M.,

745 Martin, D., and Choi, E. 2014. Multi-parameter monitoring of a slow moving landslide:

746 Ripley Slide, British Columbia, Canada. *In* Engineering Geology for Society and Territory -

747 Volume 2, Landslide Processes, IAEG  Congress, Springer Publishing, pp. 155-159

748

749 Bobrowsky P., Huntley D., Neelands P, MacLeod R, Mariampillai D, Hendry M, Macciotta

750 R, Reeves H., and Chambers J. 2017. Ripley Landslide – Canada's premier landslide field

751 laboratory. Geological Society of America, Annual Meeting Abstracts and Proceedings

752 Volume, 1 p

753

754 Bobrowsky, P., MacLeod, R., Huntley, D., Niemann, O., Hendry, M. and Macciotta, R. 2018.

755 Ensuring Resource Transport Safety: Monitoring Critical Infrastructure with UAV

756 Technology. Resources for Future Generations, Proceedings Volume and Abstracts,

757 Vancouver, Canada, 1 p

758

759 Bunce C. and Chadwick, I. 2012. GPS monitoring of a landslide for railways. In: Eberhardt

760 E, et al (eds) Landslides and Engineered Slopes - Protecting Society through Improved

761 Understanding: 1373-1379

762

763      Church, M., Ryder, J.M. 1972. Paraglacial sedimentation: a consideration of fluvial processes

764      conditioned by glaciation. Geological Society America, Bulletin 83: 3059–3072

765

766      Clague, J. and Evans, S. 2003. Geologic framework for large historic landslides in Thompson

767      River valley, British Columbia. Environmental and Engineering Geoscience **9** (3): 201-212

768

769      Cruden, D.M. and Varnes, D.J. 1996. Landslide types and processes. *In* Landslides,

770      Investigation and Mitigation. Washington Transportation Research Board, Special Report

771      **247**: 36 -75

772

773      Deblonde, C., Cocking, R.B., Kerr, D. E., Campbell, J.E., Eagles, S., Everett, D., Huntley,

774      D.H., Inglis, E., Parent, M., Plouffe, A., Robertson, L., Smith, I.R. and Weatherston, A. 2018.

775      Surficial Data Model: the science language of the integrated Geological Survey of Canada

776      data model for surficial geology maps. Geological Survey of Canada, Open File 8236, (ed.

777      version 2.3.14), 50 p, (2 sheets)

778      Drysdale, C.W. 1914. Geology of the Thompson River valley below Kamloops Lake, B.C. *In*

779      1912 Summary Report, Geological Survey, Department of Mines Sessional Paper, **26**: 115-

780      150

781

782      Eshraghian, A., Martin, C. and Cruden, D. 2007. Complex earth slides in the Thompson

783      River Valley, Ashcroft, British Columbia. Environmental and Engineering Geoscience XIII:

784      161-181

785

786    Eshraghian, A., Martin, C. and Morgenstern, N. 2008. Movement triggers and mechanisms of

787    two earth slides in the Thompson River Valley, British Columbia, Canada. Canadian

788    Geotechnical Journal, **45**: 1189-1209

789

790    Evans, S.G. 1984. The 1880 landslide dam on Thompson River, near Ashcroft, British

791    Columbia. In: Current Research, Part A: Geological Survey of Canada Paper 84-1A: 655–658

792

793    Fredlund, D.G., Morgenstern, N.R. and Widger, R.A. 1976. The shear strength of unsaturated

794    soils. Canadian Geotechnical Journal, **13**: 261-275

795

796    Fulton, R.J. 1969. Glacial Lake History, Southern Interior Plateau, British Columbia.

797    Geological Survey of Canada, Paper 69-37, 14 p

798

799    Gordey, S.P., Geldzetzer, H.H.J., Morrow, D.W., Bamberm, E.W., Henderson, C.M.,

800    Richards, B.C., McGugan, A., Gibson, D.W. and Poulton, T.P. 1991. Ancestral North

801    America, Part A. *In* Upper Devonian to Middle Jurassic assemblages, Chapter 8 of Geology

802    of the Cordilleran Orogen in Canada, Geology of Canada, Geological Survey of Canada, **4**:

803    219-327

804

805    Hebda, R.J. 1982. Postglacial history of grasslands of southern British Columbia and adjacent

806    regions. *In* Grassland Ecology and Classification Symposium Proceedings. British Columbia

807    Ministry of Forests, pp. 157-191

808

809    Hebda, R.J. 1995. British Columbia vegetation and climate history with focus on 6 ka B.P.

810    Geographic Physique et Quaternaire, **49**: 55-79

811

812    Hendry, M., Macciotta, R. and Martin, D. 2015. Effect of Thompson River elevation on

813    velocity and instability of Ripley Slide. Canadian Geotechnical Journal, **52** (3): 257-267

814

815    Huntley, D. and Bobrowsky, P. 2014.Surficial geology and monitoring of the Ripley Slide,

816    near Ashcroft, British Columbia, Canada. Geological Survey of Canada, Open File 7531, 21

817    p

818

819    Huntley, D., Bobrowsky, P., Zhang, Q., Zhang, X., Lv, Z., Hendry, M., Macciotta, R.,

820    Schafer, M., Le Meil, G., Journault, J. and Tappenden, K. 2016. Application of Optical Fibre

821    Sensing Real-Time Monitoring Technology at the Ripley Landslide, near Ashcroft, British

822    Columbia, Canada. Canadian Geotechnical Society, GeoVancouver 2016 Annual Meeting

823    Proceedings Volume, 13 p

824

825    Huntley, D., Bobrowsky, P., Parry, N., Bauman, P., Candy C. and Best, M. 2017a. Ripley

826    Landslide: the geophysical structure of a slow-moving landslide near Ashcroft, British

827    Columbia, Canada. Geological Survey of Canada, Open File 8062, 59 p

828

829    Huntley, D., Bobrowsky, P. and Best, M. 2017b. Combining terrestrial and waterborne

830    geophysical surveys to investigate the internal composition and structure of a very slow-

831    moving landslide near Ashcroft, British Columbia, Canada. *In* Landslide Research and Risk

832    Reduction for Advancing Culture and Living with Natural Hazards - Volume 2, 4th World

833    Landslide Forum (ICL-IPL), Springer Nature, 15 p

834

835  Huntley, D., Bobrowsky, P., Zhang, Q,, Zhang, X, and Lv, Z. 2017c. Fibre Bragg Grating and

836  Brillouin Optical Time Domain Reflectometry Monitoring Manual for the Ripley Landslide,

837  near Ashcroft, British Columbia. Geological Survey of Canada, Open File 8258, 66 p

838

839  Huntley, D., Bobrowsky, P., Hendry, M., Macciotta, R. and Best, M. 2019a. Multi-technique

840  geophysical investigation of a very slow-moving landslide near Ashcroft, British Columbia,

841  Canada. Journal of Environmental and Engineering Geophysics, **24** (1): 85-108

842

843  Huntley, D., Bobrowsky, P., Hendry, M., Macciotta, R., Elwood, D., Sattler, K., Best, M.,

844  Holmes, J., Chambers, J., Meldrum, P. and Wilkinson, P. 2019b. Application of multi-

845  dimensional electrical resistivity tomography datasets to investigate a very slow-moving

846  landslide near Ashcroft, British Columbia, Canada. Landslides, **16** (5):1033-1042

847

848  Huntley, D., Bobrowsky, MacLeod R., Cocking, R., Joseph, J., P., Slatter, C., Elwood, D.,

849  Holmes, J., Chambers, J., Meldrum, P., Wilkinson, Hendry, M., and Macciotta, R. 2019c.

850  PRIME installation in Canada: protecting national railway infrastructure by monitoring

851  moisture in an active slow-moving landslide near Ashcroft, British Columbia. Geological

852  Survey of Canada, Open File 8548, 1 poster

853

854  Journault, J., Macciotta, R., Hendry, M., Charbonneau, F., Huntley, D. and Bobrowsky, P.

855  2018. Measuring displacements of the Thompson River valley landslides, south of Ashcroft,

856  B.C., Canada, using satellite InSAR. Landslides **15** (4): 621-636.

857

858  Le Meil, G. 2017. Characterization of a landslide-prone glaciolacustrine clay from the

859  Thompson River Valley near Ashcroft, British Columbia. Department of Civil and

860   Environmental Engineering, University of Alberta, Masters of Science in Geological

861   Engineering, 182 p

862

863   Macciotta, R., Hendry, M., Martin, D., Elwood, D,, Lan, H., Huntley, D., Bobrowsky, P.,

864   Sladen, W., Bunce, C., Choi, E. and Edwards, T. 2014. Monitoring of the Ripley Slide in the

865   Thompson River Valley, B.C. Geohazards 6 Symposium, Proceedings and Abstracts Volume,

866   Kingston, Ontario, Canada, 1 p

867

868   Mathewes, R.W. and King, M. 1989. Holocene vegetation, climate, and lake-level changes in

869   the Interior Douglas-Fir biogeoclimatic zone, British Columbia. Canadian Journal of Earth

870   Sciences, **26**: 1811-1825

871

872   Merritt, A., Chambers, J., Murphy, W., Wilkinson, P., West, L., Gunn, D., Meldrum, P.,

873   Kirkham, M. and Dixon, N. 2014. 3D ground model development for an active landslide in

874   Lias mudrocks using geophysical, remote sensing and geotechnical methods. Landslides, **11**

875   (4): 537-550

876

877   Monger, J.W.H. and McMillan, W.J. 1989. Geology, Ashcroft, British Columbia (92 I).

878   Geological Survey of Canada, Map 42-1989, Scale 1:250,000

879

880   Nicholson, A., Hamilton, E., Harper, W.L., Wikeen, B.M. Bunchgrass Zone – Chapter 8. In:

881   Meidinger, D. and Pojar, J. 1991. Ecosystems of British Columbia. B.C. Ministry of Forests,

882   Special Report 6: 125-137

883

884    Piegari, E. and Di Maio, R. 2013. Estimating soil suction from resistivity. Natural Hazards

885    Earth Systems Science, **13**: 2369-2379

886

887    Porter, M., Savigny, K., Keegan, T., Bunce, C. and MacKay, C. 2002. Controls on stability of

888    the Thompson River landslides. In: Proceedings of the 55th Canadian Geotechnical

889    Conference: Ground and Water – Theory to Practice, Canadian Geotechnical Society, pp.

890    1393-1400

891

892    RES3DINV (2017 [URL]) Rapid 3-D Resistivity & IP inversion using the least-squares

893    method, Geoelectrical Imaging 2D & 3D Geotomo Software Version 3.14, Available from

894    www.geotomosoft.com [accessed April, 2019]

895

896    Ryder, J.M. 1976. Terrain inventory and Quaternary geology, Ashcroft, British Columbia.

897    Geological Survey of Canada, Paper 74-79, 17 p

898

899    Ryder, J.M., Fulton, R.J. and Clague, J.J. 1991. The Cordilleran Ice Sheet and the Glacial

900    Geomorphology of Southern and Central British Colombia. Géographie physique et

901    Quaternaire, **45** (3): 365–377

902

903    Schafer, M., Macciotta, R., Hendry, M., Martin, D., Bobrowsky, P., Huntley, D., Bunce, C.

904    and Edwards, T. 2015. Instrumenting and Monitoring a Slow Moving Landslide. GeoQuebec

905    2015 – Challenges from North to South, 7 p

906

907    Stanton, R.B. 1898. The great land-slides on the Canadian Pacific Railway in British

908    Columbia. Proceedings of Civil Engineers **132** (2): 1–48

909

910    Uhlemann, S., Chambers, J., Wilkinson, P., Maurer, H., Merritt, A., Meldrum, P., Kuras, O.,

911    Gunn, D. and Dijkstra, T. 2017. Four-dimensional imaging of moisture dynamics during

912    landslide reactivation. Journal of Geophysical Research (Earth Surface), **122**: 398-418

913

914

915

916

917

**Tables**

**Table 1** Hydrogeological characteristics of Ripley Landslide.

| Hydro-geological Unit (thickness, m) | Earth material textures (and Porosity) Intercrystalline porosity Intergranular porosity Vugular porosity **H** (high porosity), **M** (moderate porosity) or **L** (low porosity) | Penetrative structures (and Porosity) Fracture porosity **H** (high porosity), **M** (moderate porosity) or **L** (low porosity) | Drainage (and Permeability) Rate at which surface water and groundwater flows through unit: **H** (high permeability), **M** (moderately permeability) or **L** (low permeability) |
|---|---|---|---|
| **Unit 10** Anthro-pogenic materials (<2 m – 5 m) | Intergranular porosity (**H**) Open framework, clast-supported cobble and boulder ballast | Fracture porosity (**H**) • Displacement of concrete lock-blocks • Sub-vertical crescentic tension cracks in ballast | Rapidly drained (**H**) Percolating surface water quickly removed downslope during heavy or prolonged rainfall |
| **Unit 9** Alluvial sediments (<2 m) | Intergranular porosity (**H**) Open framework, clast-supported boulders and sand | | Rapidly drained (**H**) Percolating surface water quickly removed downslope during heavy or prolonged rainfall; permanently saturated at shallow depth (<2 m) |
| **Unit 8** Hillslope colluvial sediments (<2 m) | Intergranular porosity (**H**) Talus blocks veneer steep bedrock slopes  Stratified diamicton and clast-supported cobbles, boulders with interstitial sand and silt veneer unconsolidated slopes | Fracture porosity (**H**) • Sub-vertical crescentic tension cracks oriented N-S on slide body | Rapidly drained (**H**) Percolating surface water and groundwater quickly removed downslope, with subsurface flow during heavy or prolonged rainfall |
| **Unit 7** Alluvial fan sediments (<2 m) | Intergranular porosity (**M**) Basal interbedded stratified diamicton and open framework, clast-supported cobble-gravel, fining upward to massive sand and silt; cm-thick beds sub-parallel to surface slopes from 3° to 8° (fans) and >8° to <12° (cones) | Fracture porosity (**H**) • Sub-vertical crescentic tension cracks oriented N-S on slide body | Well drained (**M**) Percolating surface water readily removed downslope, with subsurface seepage during heavy or prolonged rainfall |
| **Unit 6** Glaciofluvial sediments (2 m to >5 m) | Intergranular porosity (**H**) Massive and crudely stratified, open framework, clast-supported boulder and sand-rich gravel beds, m-thick beds | | Rapidly drained (**H**) Percolating surface water and groundwater readily removed downslope, with subsurface flow during heavy or prolonged rainfall |
| **Unit 5** Glacio-lacustrine sediments (<2 m to 5 m) | Intergranular porosity (**M**) Pebble-rich sand; cm-thick interbeds | Fracture porosity (**M**) Rhythmically interbedded silt, clay and diamicton, cm-thick with: • Sub-vertical N-S unloading fractures parallel to exposed slope • Sub-vertical crescentic tension cracks oriented N-S on slide body • Fissile partings parallel to bedding, dipping W into bedrock basin | Imperfectly drained (**L**) Seepage from exposed porous sand-rich interbeds indicated by salt crusts form at surface during summer months along the railway and river embankments; at depth, fractures become saturated during prolonged rainfall |
| **Unit 4** Glacial till sediments (2 m to 6 m) | Vugular porosity (**L**) Massive, matrix-supported diamicton composed of silt, clay and boulders, isolated weathered clasts and sand-filled voids; m-thick beds | Fracture porosity (**M**) • Sub-vertical unloading fractures sub-parallel to exposed slopes, oriented N-S • Sub-vertical crescentic tension cracks oriented N-S on slide body • Sub-horizontal shear surfaces below 270 m elevation, dipping W into bedrock basin | Imperfectly drained (**L**) Fractures allow downward and subsurface flow of groundwater; fractures become saturated at depth during prolonged rainfall and during high river stage |
| **Unit 3** Glacio-lacustrine sediments (5 m to >15 m) | Intergranular porosity (**M**) Sand and gravel; cm-thick interbeds; uncommon | Fracture porosity (**L**) Rhythmically interbedded clay and silt and diamicton, mm-thick with: • Sub-vertical N-S oriented unloading fractures parallel to exposed slope • Sub-vertical crescentic tension cracks oriented N-S on slide body | Poorly drained (**L**) Sub-surface sediments remain undersaturated for much of year, except during prolonged rainfall, sustained confined groundwater flow and during high river stage |

| | | | |
|---|---|---|---|
| | • Contorted bedding and loading structures<br>• Fissile partings parallel to bedding, dipping W into bedrock basin<br>• Sub-horizontal shear surfaces below 260 m elevation, dipping W into bedrock basin | | |
| **Unit 2**<br>Glacio-lacustrine sediments<br>(<2 m to 6 m) | Intergranular porosity (**M**)<br>Sand, gravel, stratified clast-supported diamicton; cm-thick interbeds | Fracture porosity (**L**)<br>Silt, clay and matrix-supported diamicton; cm-thick; with:<br>• Fissile partings along bedding planes dipping W into bedrock basin | Imperfectly drained (**L**)<br>Fissile, bedded sediments remain saturated for much of year |
| **Unit 1b**<br>Rhyolite[1] and Volcaniclastic rocks[2]<br>(>2 m) | Vugular porosity (**L**)<br>[2]Welded, clast-supported agglomerate<br><br>Intercrystalline porosity (**L**)<br>[1]Fine-grained, flow-banded crystalline igneous rock<br>[1,] | Fracture porosity (**M**)<br>• [2]Bedding planes, *<20° NNE*<br>• [1,2]Dominant fracture sets, *NW – SW*<br>• Weathering rinds along fracture surfaces<br>• Fractures sealed at depth | [1,2]Well drained (**M**)<br>Shallow bedrock fractures and bedding planes allow downward and subsurface flow of groundwater<br>[1,2]Poorly drained (**L**)<br>At depth, fractures saturated for much of year, or too tight for water flow |
| **Unit 1a**<br>Andesite<br>(>2 m) | Intercrystalline porosity (**L**)<br>Fine-grained, massive crystalline igneous rock | Fracture porosity (**M**)<br>• Dominant fracture sets, *E – NW*<br>• Weathering rinds along fracture surfaces<br>• Fractures sealed at depth | Well drained (**M**)<br>Shallow bedrock fractures and bedding planes allow downward and subsurface flow of groundwater<br>Poorly drained (**L**)<br>At depth, fractures saturated for much of year, or too tight for water flow |

921

922

923

924 **Table 2** Summary of modelled terrestrial and waterborne ERT, FEM, GPR and Seismic

925 properties of surficial units and bedrock at Ripley Landslide; * groundwater seeps / **

926 groundwater in fractures, partings and porous beds / *** downward percolating surface

927 waters; GPR reflectors, P – point, L – linear, S- strong, M – moderate, W – weak.

| Hydro-geological Unit | Earth Material Description; structure; drainage | T-ERT Ωm | W-ERT Ωm | T-FEM Modelled conductivity mS m⁻¹ / *Resistivity Ωm* | W-EM Modelled conductivity mS m⁻¹ Bathymetry corrected / *Resistivity Ωm* | T-GPR, W-GPR Origin, character, strength of reflectors | Seismic Refraction P-wave velocity m s⁻¹ | Shear Wave Velocity m s⁻¹ |
|---|---|---|---|---|---|---|---|---|
| **Unit 10** */*** Anthro-pogenic | Cobble and boulder ballast; rapidly-drained | <500 | - | <5 *>200* | - | Boulders P, S Unit contact L, W | 250 - 600 | 240 - 280 |
| **Unit 9** */*** Alluvial *May contain ground-water seeps* | Boulders and sand; rapidly drained; saturated | <500 | 100 - 450 | <5 *>200* | 30 – 60 *33 - 17* | Boulders P, S Unit contact L, W | 600 - 3500 | 240 - 280 |
| **Unit 8** */*** **C**olluvial | Blocks, gravel, sand, clast-supported diamicton; rapidly-drained | <500 | - | <20 *>50* | - | Boulders P, M - S Unit contact L, W | 250 - 600 | 100 - 240 |
| **Unit 7** */*** Alluvial | Sand, silt and minor gravel; well-drained | 125 - 500 | - | <20 *>50* | - | Basal contact L, W | 250 - 600 | 100 - 200 |
| **Unit 6 *** Glaciofluvial | Gravel and sand; rapidly-drained | 125 - 500 | - | <20 *>50* | - | Boulders P, M Basal contact L, W | 250 | 100 - 280 |
| **Unit 5** */** Glacio-lacustrine | Silt and clay; deformed; imperfectly-drained | <125 | - | >20 *<50* | - | Groundwater L, W - M Basal contact L, W - M | 1400 – 2300 | 240 - 300 |
| **Unit 4** **/*** Till | Silt-clay matrix-supported diamicton; imperfectly-drained | 125 - 500 | 25 - 150 | >20 *<50* | 15 – 30 *67 - 33* | Boulders P, M Groundwater L, W - M Basal contact L, W - M | 400 - 600 | 280 - 380 |
| **Unit 3** */** Glacio-lacustrine | Clay and silt; deformed; stiff to hard; poorly-drained | <125 | 25 – 100 | >20 *<50* | 15 – 30 *67 - 33* | Groundwater L, W - M Basal contact L, M - S | 1400 – 2300 | 300 - 500 |
| **Unit 2** */** Colluvial | Clay, poorly-drained, stiff to hard; and blocks, gravel, sand, clast-supported diamicton; imperfectly-drained | <500 | 150 – 500 | <20 *>50* | 15 – 30 *67 - 33* | Basal contact L, M - S | 600 - 3500 | 380 - 500 |
| **Unit 1** **/*** Bedrock *May contain* | Andesite, rhyolite and pyroclastic beds; weathered, | >500 | 1,000 - >3,000 | <5 *>200* | <15 *>67* | No internal reflectors | 3500 - 4000 (weathered) | 500 - 700 |

| *ground- water* | fractured; well- drained | >4000 (pristine) |
| --- | --- | --- |

928

929

930

931

932

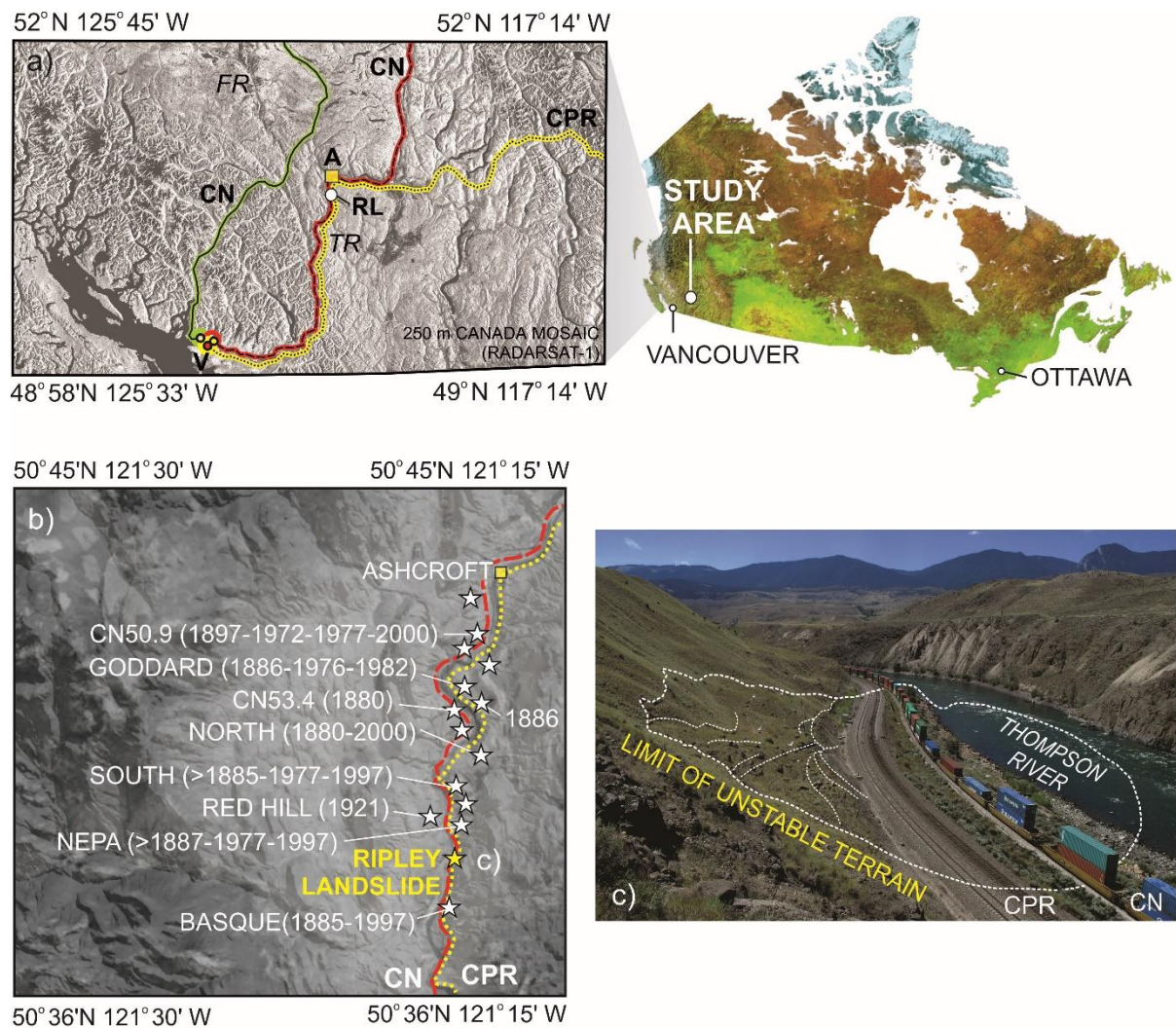| *ground- water* | fractured; well- drained | >4000 (pristine) |
| --- | --- | --- |

933

# Figures



934
935
936 **Fig. 1** The study area. a) Rail transportation corridors in southwestern British Columbia with location of the
937 Thompson River valley area of interest: **A** – Ashcroft; **K** – Kamloops; **L** – Lytton; **S** – Spences Bridge; **V** –
938 Vancouver; **FR** – Fraser River; **TR** - Thompson River. b) Landslides of the Thompson River valley, with location
939 of Ashcroft, the railway transportation corridor and Ripley Landslide test site. c) Overview of the test site
940 highlighting the approximate limit of unstable terrain and submerged slide toe.
941

942

**Fig. 2** Hydrogeological units of Ripley Landslide. a) Unit 1a- andesite: fine-grained crystalline igneous rock with dominant fractures 040º/076º/E (278 m elevation), 074º/50º/NNW, 136º/78º/W, 178º/28º/E. b) Unit 1b - rhyolite and pyroclastic volcanic rock: strike/dip/dip-direction 104º/18º/E (350 m elevation). c) Unit 2 – colluvial sediments: interbedded clast-supported diamicton, sand and gravel overlying fractured bedrock (unit 1), ca. 276 m elevation. d) Unit 3 - glaciolacustrine sediments: rhythmically interbedded clay, silt and sand with rare dropstones; sub-till (unit 4) soft-sediment indicates glacial deformation, ca. 278 m elevation. e) Unit 4 – lodgement till: massive, matrix-supported diamicton overlain by a veneer of hillslope colluvium (unit 8) exposed in headscarp; at 280 m elevation. f) Unit 5 - glaciolacustrine sediments: interbedded silt and clay overlying till (unit 4), silt-rich beds appear lighter; bedding-parallel fissility and vertical slope relaxation fractures formed in exposed in railway embankment. g) Unit 6 - glaciofluvial sediments: cobble gravel and sand; moderately steep slope (25 º - 32º) is

953 gullied and drains a 340 m - 350 m elevation terrace abutting against bedrock (unit 1b). h) Unit 7 - alluvial fan
954 sediments: silt, sand and gravel deposited on outwash and till as terraced fans with slopes up to 12º; indicate falling
955 base-levels in the Thompson River valley during early Holocene. i) Unit 8 - colluvial sediments: erratic boulders,
956 glaciofluvial cobbles and sand remobilized by debris fall, soil creep and surface runoff on slopes ranging from 25º
957 slope above the headscarp to 12º across the main slide body; on steeper portions of the slope (up to 32º), talus
958 blocks are derived from frost shattered rhyolite and volcaniclastic rock. j) Unit 9 - alluvial floodplain sediments:
959 boulders, cobbles and sand, sparse vegetation growth dominated by horsetails indicating zone of seepage across
960 the landslide toe. k) Unit 10 - anthropogenic features: boulder-rich track ballast overlying alluvial floodplain on
961 the landslide toe; CN (top left) and CPR tracks (centre); l) Unit 10 - lock-block retaining wall separating CPR
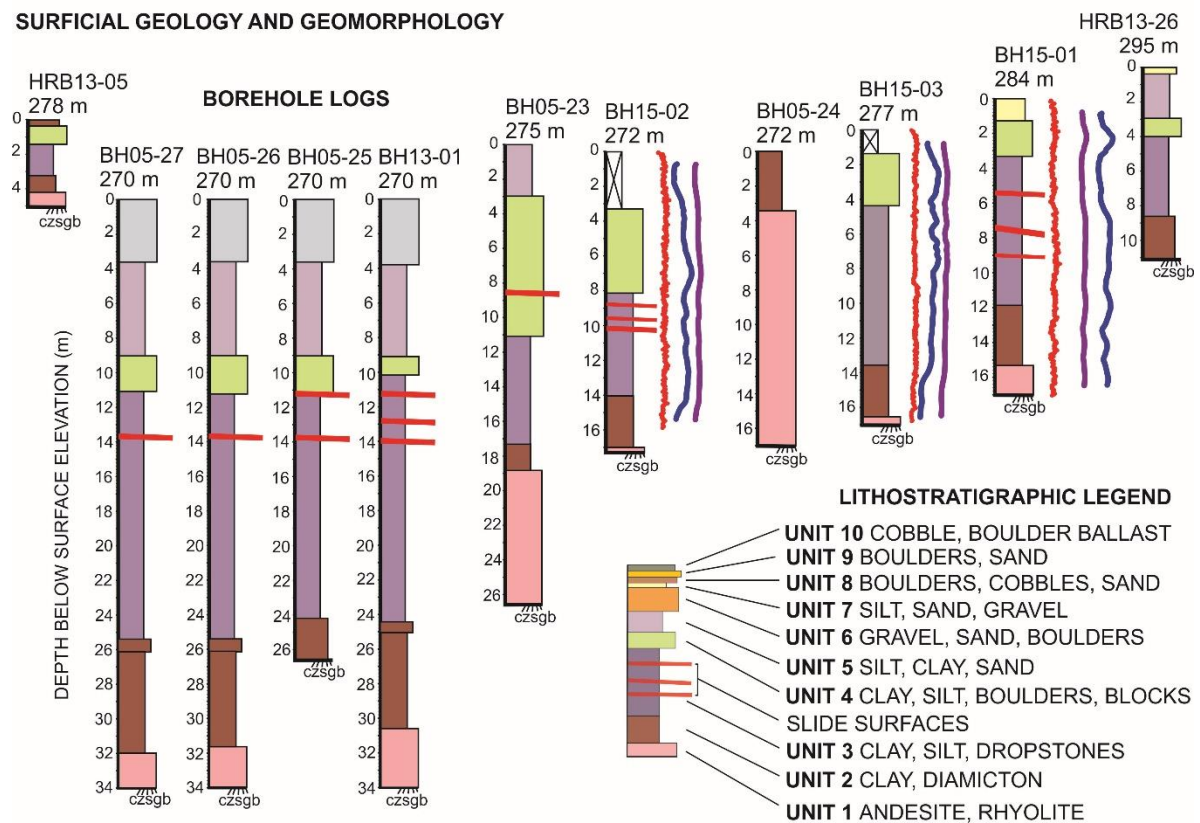962 (above left) and CN tracks (right).

963
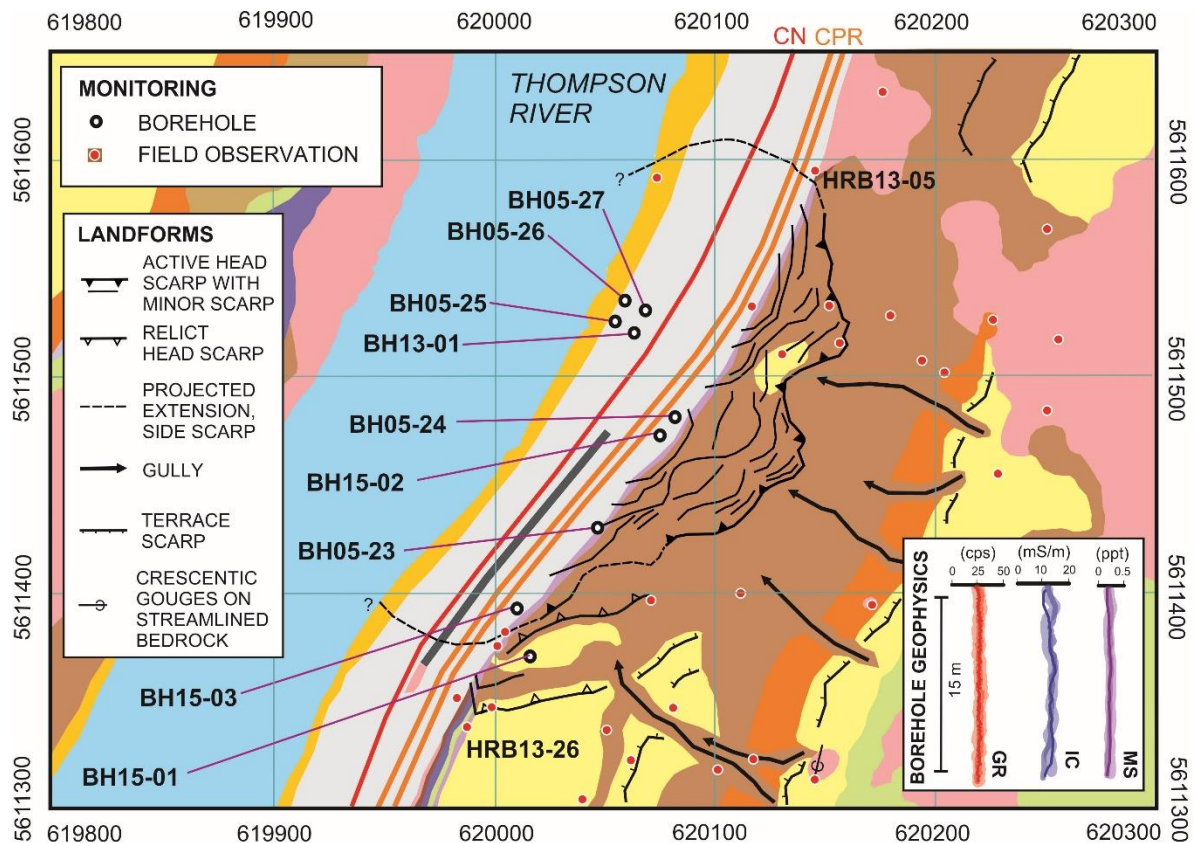
**Fig. 3** Surficial hydrogeological units and landforms of Ripley Landslide and adjacent terrain, showing location of boreholes and field observations; lock-block retaining wall – grey line. Borehole geophysical logging and data processing by Frontier Geosciences Inc.
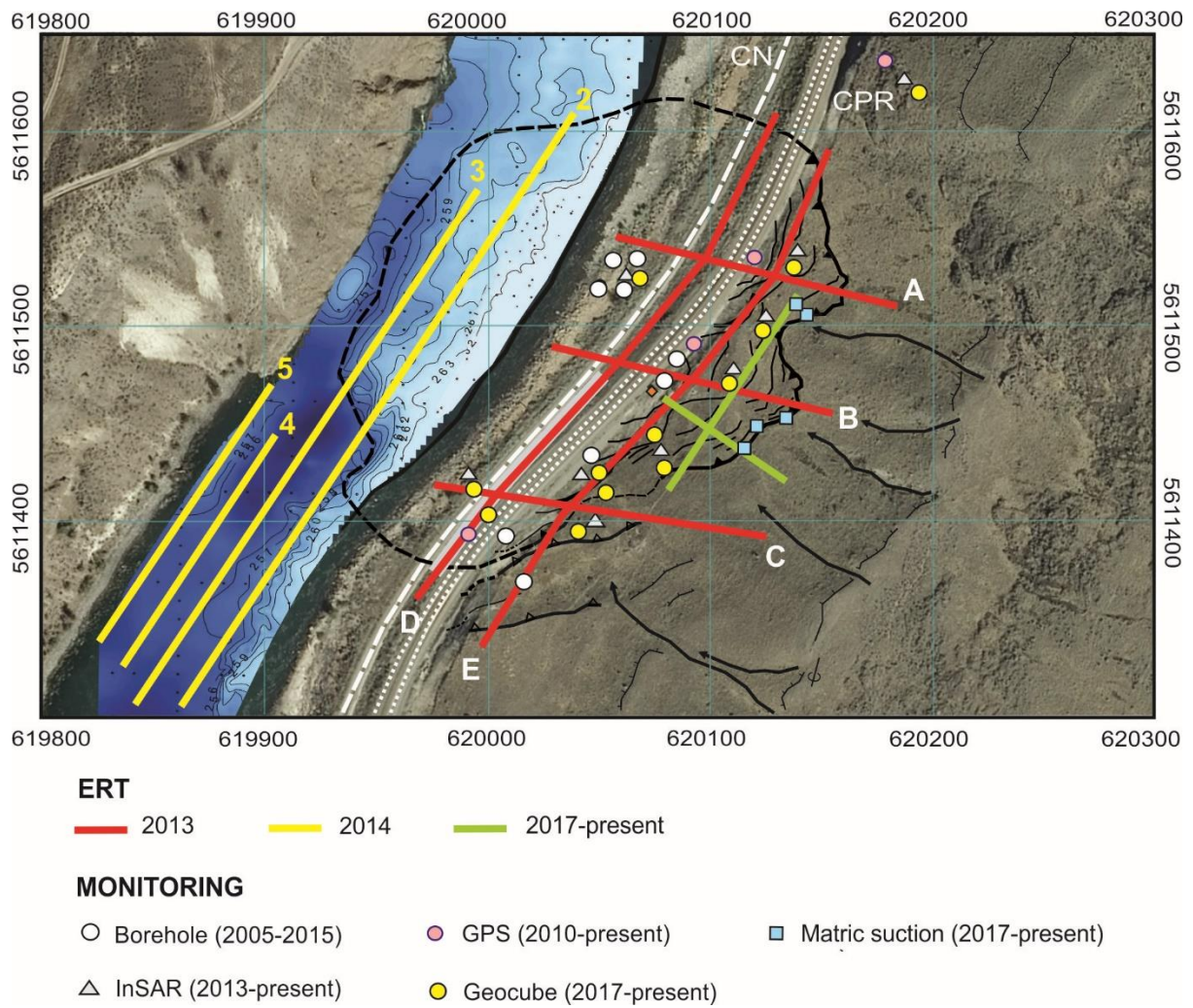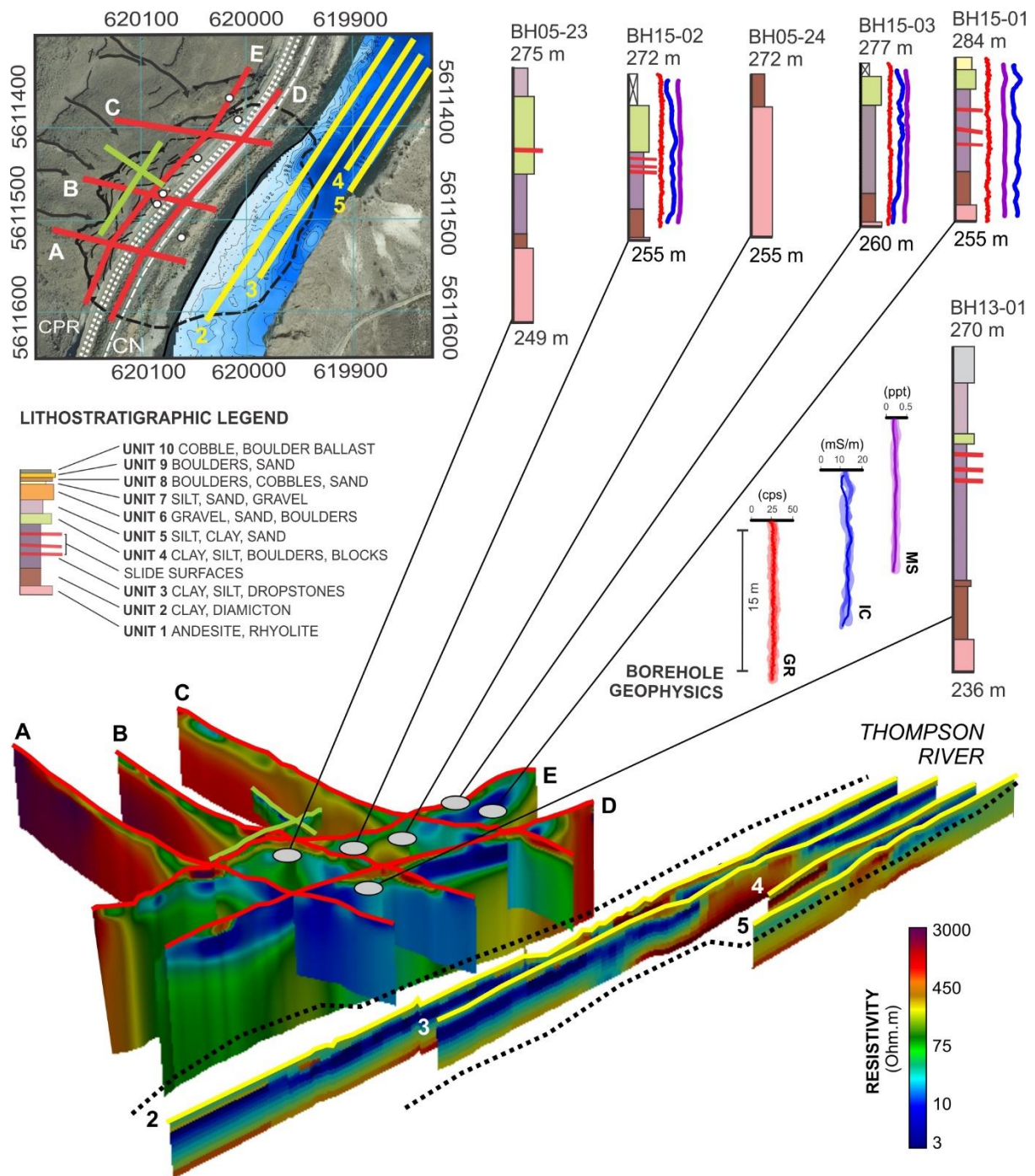
**Fig. 4** Geophysical transects for November 2013 (red lines), November 2014 (yellow lines), and PRIME installation, beginning in November 2017 (green lines); other monitoring components shown include positions of logged boreholes (2005-2015), InSAR corner reflectors (2013 - present) and permanent GNSS stations (2010 – present).

972

**Fig. 5** Terrestrial ERT pseudosections (red transect lines A, B, C), waterborne ERT pseudosections (yellow transect lines 2, 3, 4, 5) and PRIME installation (green transect lines). Location of boreholes shown in relation to transect lines. Gamma radiation measured in counts per second (cps), induced conductivity measured in milliSiemens/m (mS/m) and magnetic susceptibility in parts per thousand (ppt). Also shown, location of elevated terrain conductivity readings located on submerged slide toe. Landslide extent (approximate) shown as dashed black lines on inset map.
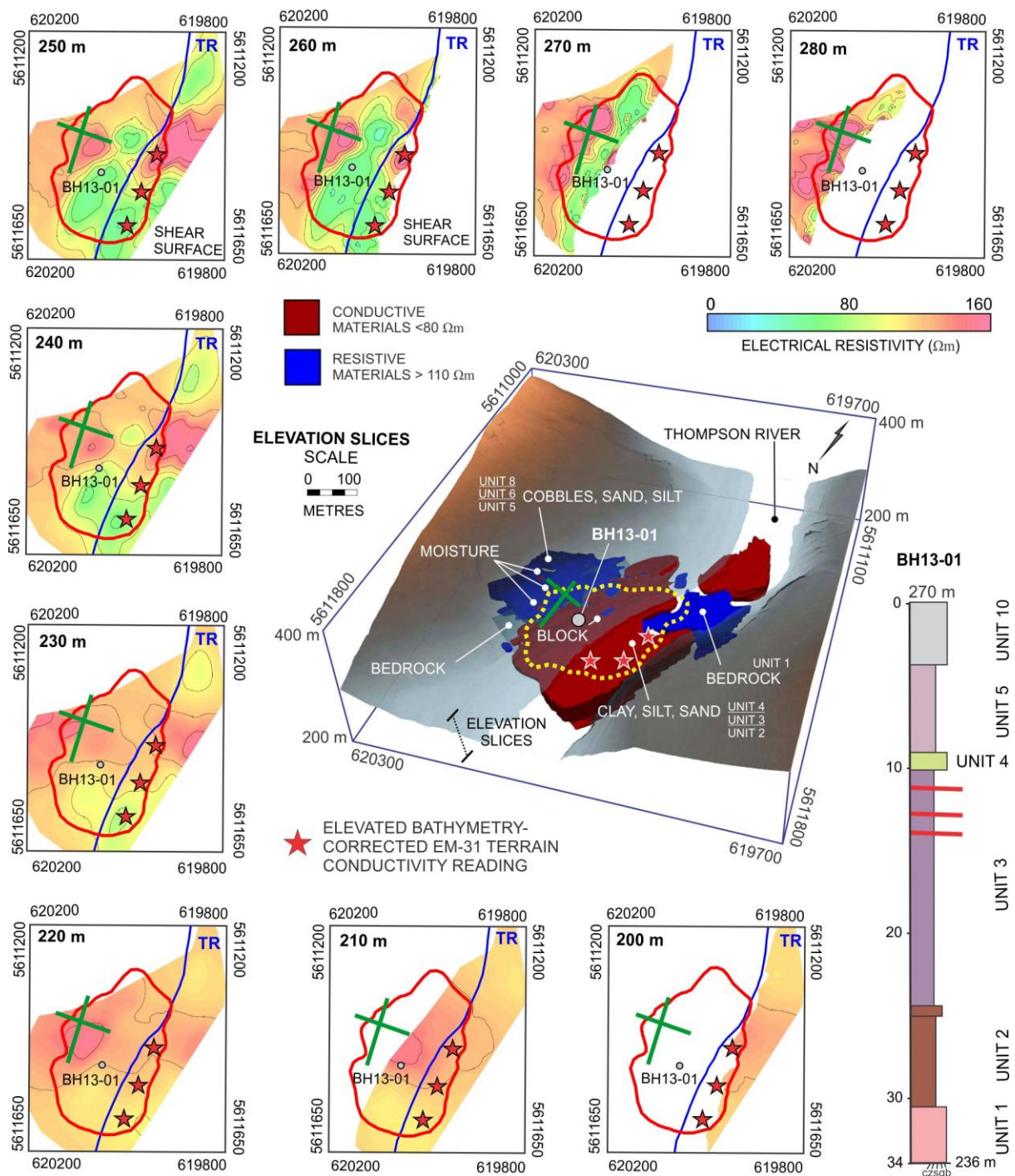
979

**Fig. 6** Electrical resistivity tomographic depth slices of Ripley Landslide. Location of BH13-01 shown; graphic log captures changes in hydrogeological units at depth near the centre of the slide body. Solid blue line – east bank of Thompson River (**TR**). Solid green line - PRIME array. Red stars indicate elevated bathymetry-corrected EM terrain conductivity interpreted as artesian groundwater discharge zones exposed by river erosion. Data processing by Frontier Geosciences Inc.
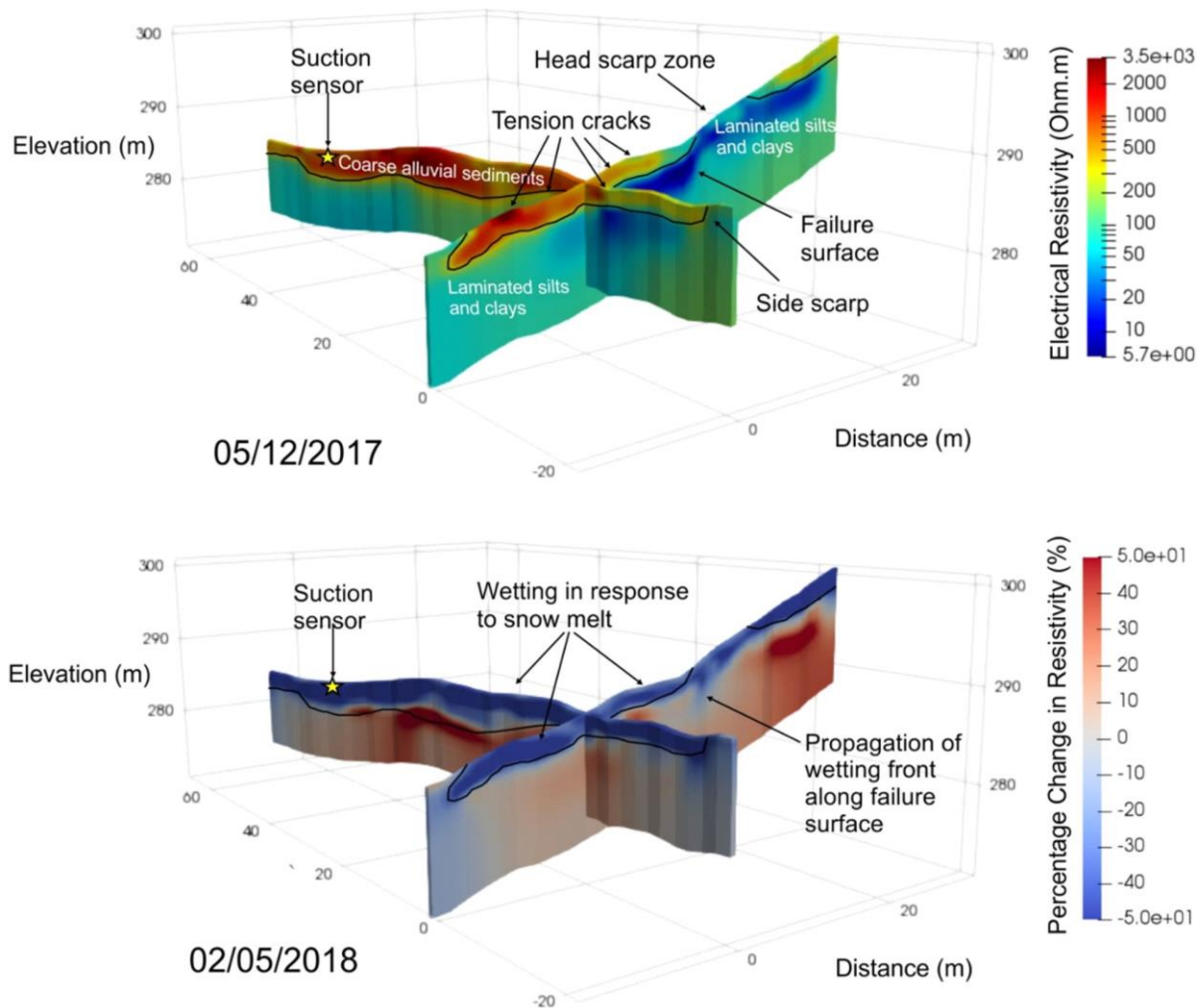
**Fig. 7** Electrical resistivity tomography images generated from the PRIME data collected on the Ripley landslide. The baseline image (December 05, 2017) highlights the lithological units present on site and shows key geomorphological features including failure surfaces and tension cracks. The image from May 02, 2018 shows the percentage change in resistivity from the baseline image, highlighting changes which took place following the onset of snowmelt on the site. Suction sensor locations are marked by the yellow stars. The suction sensors (yellow star) are located at 0.3 m, 0.6 m, 0.9 m, 1.2 m and 2 m below the surface.

992
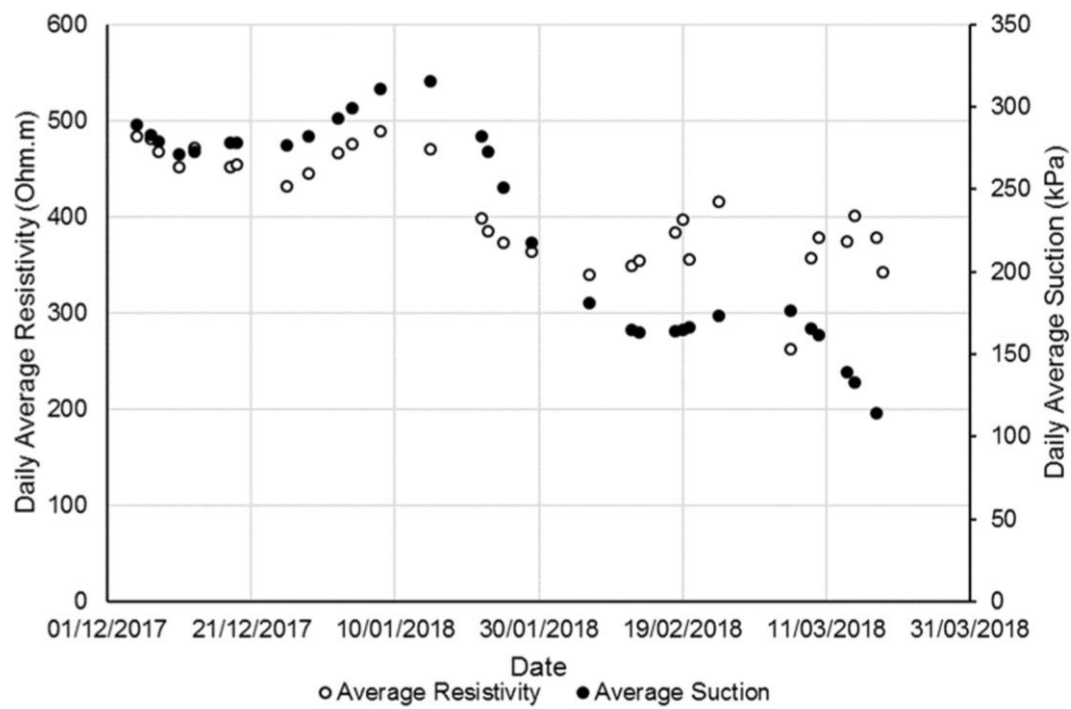
**Fig. 8** Relationship between resistivity and suction for the Ripley landslide head scarp. The average daily resistivity is the average resistivity of cells of the PRIME model (**Fig. 7**) proximal to the suction sensors (within 1 m distance). The suction sensors are located at 2, 3, 4, and 6.5 ft depth from the surface, and their location relative to the PRIME ERT lines is shown in **Fig. 7**.